Energy Conversion and Management: X 30 (2026) 101846

Contents lists available at ScienceDirect

Energy Conversion and Management: X

journal homepage: www.sciencedirect.com/journal/energy-conversion-and-management-x

Exergy-based pore-network optimization of gas diffusion layers for enhanced efficiency in proton exchange membrane fuel cells

Sa'ed Rawashdea [a,*], Mohammad R. Almajali [b], Ahmed M. Salem [a], Akram E. Zeid [a], Nathan Kawansson [c], Donald Paterson [a]

[a] Marine Engineering Technology, Sharjah Maritime Academy, Sharjah, United Arab Emirates
[b] Defence and Security Program, Rabdan Academy, Abu Dhabi, United Arab Emirates
[c] Maritime Logistics and Supply Chain Management (MLSCM), Sharjah Maritime Academy, Sharjah, United Arab Emirates

ARTICLE INFO

Keywords:
Exergy-Based Optimization
Pore-Network Modelling
Gas Diffusion Layer Engineering
Entropy Generation Minimization
Thermodynamic Microstructural Design

ABSTRACT

This work introduces a new exergy-based pore-network optimization framework of thermodynamic engineering Gas Diffusion Layers (GDLs) in Proton Exchange Membrane Fuel Cells (PEMFCs). In contrast to the traditional continuum or fully transport-based models, the proposed methodology will combine stochastic pore-network modelling with local entropy generation mapping and multi-objective optimization with the use of the NSGA-II to directly minimize the exergy destruction and to maximize the electrochemical performance. Mass diffusion, viscous dissipation, heat transfer, and electrochemical reactions irreversibility's are solved at the pore scale, which allows spatial localization of thermodynamic hotspots. Findings show that optimal microstructures, which minimize the destruction of exergy by 18–24%, increase peak exergy efficiency by about 11%, and increase current density at 0.6 V by almost 68%. Entropy generation through diffusion was found to be the most important irreversibility mechanism, contributing over 45% of total exergy loss at high-load operation, and thus topology control of pores is indeed very important. Multi-dimensional response surfaces provided a narrow optimal design window at porosity in the range of 0.63–0.72 and tortuosity in the range of 1.5–1.9 at which the penalties associated with transport or structure dominate. The combined thermodynamic-microstructural optimization guarantees a direct quantitative connection between pore level topology and second-law performance, which offers a fresh design paradigm of high-efficiency and durability-improved PEMFC infrastructures.

1. Introduction

Global energy demand continues to rise due to industrial growth, population expansion, and the rapid electrification of transportation and infrastructure. The International Energy Agency (IEA) has repeatedly emphasized that achieving net-zero emission targets by mid-century requires deep decarbonization of the energy sector [1–12]. Although renewable energy sources such as solar and wind have achieved significant progress, their intermittency necessitates efficient energy storage and conversion technologies. In this context, hydrogen has emerged as a strategic energy carrier capable of supporting decarbonization across transportation, stationary power generation, and marine applications [1,13–17]. Its high gravimetric energy density and environmentally benign by-product (water) make it particularly attractive for sustainable energy systems.

Among hydrogen conversion technologies, (PEMFCs) have gained considerable attention due to their high-power density, rapid start-up, low operating temperature, and suitability for dynamic load conditions. Early pioneering work by Zawodzinski and Bernardi established the foundation for coupled transport–electrochemical modelling, enabling a deeper understanding of performance limitations arising from mass transport and ohmic losses [18,19]. subsequent studies, including those by Wang and Chen, further advanced PEMFC modelling by emphasizing the multi-physics interactions among electrochemistry, heat transfer, and two-phase flow phenomena[14,20–22].

Despite these advancements, PEMFC efficiency remains constrained by irreversible losses occurring across multiple scales, including activation polarization, ohmic resistance, and concentration overpotentials. Studies by Weber demonstrated the critical role of membrane hydration and water transport in determining electrochemical efficiency and durability [23–28]. Similarly, Litster highlighted the importance of microstructural characteristics of porous components-particularly the Gas Diffusion Layer (GDL)-in governing reactant distribution and water

* Corresponding author.
E-mail address: saad.alrwashdeh@sma.ac.ae (S. Rawashdea).

https://doi.org/10.1016/j.ecmx.2026.101846
Received 26 February 2026; Received in revised form 6 April 2026; Accepted 9 April 2026
Available online 12 April 2026

Nomenclature

Symbol	Description, Unit
Co2	Oxygen concentration, mol m−3
D_eff	Effective diffusivity, m2 s−1
$E_{(dest)}$	Exergy destruction rate, W
f_h	Hydrophobic fraction, –
F	Faraday constant, C mol−1
i	Current density, A m−2
I_0	Exchange current density, A m−2
K_eff	Effective thermal conductivity, W m−1 K−1
K_ef	Effective permeability, m2
N	Number of perturbation cases, –
P	Pressure, Pa
r_p	Pore radius, m
r_t	Throat radius, m
R	Universal gas constant, J mol−1 K−1
$S_{(gen)}$	Entropy generation rate, W K−1
S_l	Liquid saturation, –
T	Temperature, K
T_0	Reference temperature, K
u	Velocity vector, m s−1
Z	Coordination number, –
ΔP	Pressure drops, Pa
η	Overpotential, V
η_{ex}	Exergy efficiency, –
ε	Porosity, –
θ	Contact angle, °
μ_9	Gas viscosity, Pa.s
σ	Surface tension, N m−1
τ	Tortuosity, –

removal [29–34]. Consequently, the design and optimization of porous structures have become central to improving PEMFC performance.

The GDL serves multiple essential functions, including uniform distribution of reactant gases, removal of product water, mechanical support, and electrical conductivity. Experimental and numerical investigations by Nam demonstrated that pore morphology and wettability significantly influence capillary transport behaviour [35]. Likewise, Gostick and co-workers showed that pore size distribution and anisotropy strongly affect breakthrough pressure and liquid water saturation dynamics [36]. These findings indicate that simplified homogeneous porous assumptions are insufficient to accurately represent GDL performance.

Conventional continuum-based models typically describe the GDL using Darcy's law combined with effective diffusivity correlations derived from empirical porosity–tortuosity relationships. However, such macroscopic approaches neglect the inherent stochasticity and complex topology of fibrous media. Pore Network Modelling (PNM), originally introduced by Fatt and further developed by Blunt, provides a powerful alternative by representing porous media as interconnected networks of pores and throats [37]. Recent studies have demonstrated that pore-scale models offer improved predictive capability for two-phase flow and transport phenomena compared to volume-averaged methods [14,20].

While pore-scale modelling has significantly advanced the understanding of transport processes, most existing studies focus primarily on water management and permeability characterization, with limited attention to thermodynamic performance optimization. From a thermodynamic perspective, fuel cell inefficiencies arise from entropy generation associated with electrochemical reactions, mass diffusion, viscous dissipation, and heat transfer. The entropy generation minimization framework proposed by Li provides a rigorous basis for identifying sources of irreversibility within energy systems [38,39]. In PEMFC applications, exergy analysis has been shown to offer deeper insight into useful work potential and system losses compared to conventional efficiency metrics [4,40–42].

Non-equilibrium thermodynamic approaches based on entropy production have been introduced in recent studies to describe electrochemical systems more accurately. However, pore-scale optimization of exergy of GDL microstructures is not thoroughly studied [35,43]. The literature on exergy analysis has generally assumed the fuel cell is a lumped system, in which local thermodynamic destruction in porous transport domains is not resolved. This is a severe research gap: even though the microstructure has a strong influence on transport phenomena, its direct correlation with the amount of entropy generation and exergy destruction has not been quantitatively measured using pore-network models [44–46].

However, thermodynamic microstructural engineering provides a new direction of research. With a map of the local entropy generation in a pore-network representation, it is now possible to determine microstructural configurations that reduce irreversibility and still provide an efficient mass transport [23,47,48]. This is a philosophy that goes beyond the dominance of pure geometrical optimization to the matching of structural design to the second law of performance. By combining pore-network modelling with exergy analysis, it has become possible to design microstructural optimization objective functions that are based on physically sound principles, rather than trial-and-error approaches to their design.

Recent studies have demonstrated the effectiveness of pore-network models (PNMs) in capturing pore-scale transport phenomena within the gas diffusion layer of proton-exchange membrane fuel cells. These models have been widely used to investigate mass transport, capillary-driven liquid water dynamics, and effective transport properties in porous media. However, the application of PNMs has largely been limited to descriptive or single-objective analyses, focusing primarily on transport characterization rather than design optimization [37,46,49–51].

In contrast, the integration of pore-network modelling with multi-objective optimization frameworks remains relatively unexplored in the context of PEMFC systems. In particular, the simultaneous consideration of electrochemical performance and thermodynamic efficiency, including exergy destruction and entropy generation, has not been comprehensively addressed at the pore scale [52]. This gap highlights the need for a unified modelling and optimization approach capable of linking microstructural design parameters with both transport performance and thermodynamic irreversibility [53].

Accordingly, the present study introduces a novel framework that combines pore-network modelling, exergy-based thermodynamic analysis, and multi-objective optimization using the NSGA-II algorithm. This integrated approach enables the identification of optimal GDL microstructures that balance competing performance criteria, thereby providing new insights into the design of high-efficiency PEM fuel cell systems.

Despite the significant progress in pore-scale modelling and transport analysis of gas diffusion layers in PEM fuel cells, existing studies remain primarily focused on transport characterization or single-objective performance evaluation. In particular, the direct coupling between pore-scale microstructural design and thermodynamic irreversibility, quantified through entropy generation and exergy destruction, has not been systematically addressed. Most available exergy-based analyses are conducted at the macroscopic level and do not resolve local thermodynamic losses within the porous structure.

Therefore, this study introduces a fundamentally different approach

by integrating stochastic pore-network modelling with local entropy generation mapping and multi-objective optimization. Unlike conventional methods, the proposed framework enables the direct identification of microstructural configurations that minimize exergy destruction while simultaneously enhancing electrochemical performance. This establishes a quantitative link between pore-scale topology and second-law efficiency, providing new insights beyond traditional transport-based optimization strategies.

Consequently, this work advances the current state of the art by introducing a thermodynamically guided microstructural design methodology, offering a new paradigm for the development of high-efficiency and durability-enhanced PEM fuel cell systems.

2. Pore-Scale thermodynamic modelling and Multi-Objective optimization framework

To quantitatively link Gas Diffusion Layer (GDL) microstructure with thermodynamic performance, a fully coupled pore-scale modelling framework is developed in this study. The GDL is represented as a three-dimensional stochastic pore network consisting of pores (nodes) interconnected through throats (links), enabling explicit resolution of mass transport, momentum transfer, heat conduction, and phase interactions within the porous domain. Unlike conventional continuum homogenization approaches, the present formulation evaluates local irreversibility's at the pore scale and maps entropy generation within the network. The thermodynamic analysis is integrated with a multi-objective optimization algorithm to identify microstructural configurations that minimize exergy destruction while maximizing electrochemical performance. This section presents the governing transport equations, entropy generation formulation, and the mathematical structure of the optimization problem.

2.1. Pore network representation

The GDL microstructure is represented as a stochastic network characterized by:

- Porosity ε
- Mean pore radius r_p
- Throat radius r_t
- Coordination number Z
- Tortuosity τ
- Hydrophobic fraction f_h

The pore size distribution follows a log-normal distribution:

$$f(r_p) = \frac{1}{r_p.\sigma.\sqrt{2\pi}} \exp\left[-\frac{(\ln r_p - \mu)^2}{2\sigma^2} \right] \tag{1}$$

where r_p is the pore radius (m), $f(r_p)$ represents the probability density function of pore size distribution, μ is the mean of the logarithmic pore radius, and σ is the standard deviation of the logarithmic pore radius. The log-normal distribution is used to characterize the stochastic nature of pore size variation within the gas diffusion layer microstructure.

Permeability of each throat:

$$k_t = \frac{r_t^2}{8} \tag{2}$$

where K represents the permeability of an individual throat (m^2), r_t is the throat radius (m), and the formulation is based on the geometric characteristics of the pore–throat structure governing fluid flow within the network.

Effective permeability of the network:

$$K_{eff} = \frac{\varepsilon r_p^2}{8\tau} \tag{3}$$

where K_{eff} is the effective permeability of the pore network (m2), representing the macroscopic permeability obtained from the collective contribution of individual pore–throat conductance's within the interconnected structure.

Effective diffusivity:

$$D_{eff} = D_{O_2}.\frac{\varepsilon}{\tau} \tag{4}$$

where D_{eff} is the effective diffusivity within the porous medium ($m^2\ s^{-1}$), accounting for the influence of microstructural properties such as porosity (ε) and tortuosity (τ) on mass transport.

Mass Conservation (Oxygen Transport)

$$\nabla\cdot(-D_{eff}.\nabla C_{O_2}) = R_{O_2} \tag{5}$$

where C_{o2} is the oxygen concentration (mol m^{-3}), D_{eff} is the effective diffusivity ($m^2\ s^{-1}$), and the source term represents the rate of oxygen consumption associated with electrochemical reactions at the catalyst layer (CL) interface.

Reaction source term:

$R_{O_2} = \frac{i}{4F}$(6)where the reaction source term represents the rate of oxygen consumption (mol $m^{-3}\ s^{-1}$) associated with the electrochemical reaction at the CL interface and is directly related to the local current density through Faraday's law.

Darcy formulation:

$$\mathrm{u} = -\frac{K_{eff}}{\mu_g}\nabla P \tag{7}$$

where u is the superficial velocity vector (m s^{-1}), K_{eff} is the effective permeability of the porous medium (m^2), μ_g is the gas viscosity (Pa·s), and ∇P is the pressure gradient (Pa m^{-1}). This equation describes fluid flow through the porous structure based on Darcy's law.

Mass continuity:

$$\nabla\cdot(\rho_g.\mathrm{u}) = 0 \tag{8}$$

where the continuity equation ensures conservation of mass within the pore network by enforcing a divergence-free velocity field under steady-state conditions.

Energy Conservation

$$\nabla\cdot(-k_{eff}.\nabla T) + Q_{gen} = 0 \tag{9}$$

where T is the temperature (K), k_{eff} is the effective thermal conductivity of the porous medium (W $m^{-1}\ K^{-1}$), and the equation describes heat conduction within the gas diffusion layer.

Heat generation:

$$Q_{gen} = i(\eta_{act} + \eta_{ohm} + \eta_{conc}) \tag{10}$$

where the heat generation term represents the thermal energy produced within the system due to electrochemical reactions and irreversible processes, including activation, ohmic, and concentration losses.

Electrochemical Kinetics (Butler–Volmer Simplified)

$$i = i_0\left[\exp\left(\frac{\alpha_a.F.\eta}{R.T}\right) - \exp\left(-\frac{\alpha_c.F.\eta}{R.T}\right)\right] \tag{11}$$

where i is the local current density (A m^{-2}), i_0 is the exchange current density (A m^{-2}), η is the activation overpotential (V), T is the temperature (K), R is the universal gas constant (J $mol^{-1}\ K^{-1}$), and F is Faraday's constant (C mol^{-1}). This equation describes the electrochemical reaction kinetics governing the rate of charge transfer at the CL interface.

Capillary Pressure (Two-Phase Transport)

$$P_c = \frac{2\sigma.\cos\theta}{r_p} \tag{12}$$

where P_C is the capillary pressure (Pa), σ is the surface tension ($N\,m^{-1}$), θ is the contact angle (°), and r_p (or r_t) represents the characteristic pore or throat radius (m). This equation describes the pressure difference across the liquid–gas interface within the porous structure.

Liquid saturation evolution:

$$\frac{\partial S_l}{\partial t} + \nabla\cdot(u_l.S_l) = 0 \tag{13}$$

where S_l is the liquid saturation (–), representing the fraction of pore volume occupied by liquid water. This equation describes the evolution of liquid water within the porous structure as governed by capillary and transport processes.

Total entropy generation rate per unit volume:

$\dot{S}_{gen} = \dot{S}_{diff} + \dot{S}_{visc} + \dot{S}_{heat} + \dot{S}_{rxn} + \dot{S}_{PC}$ (14).where $S_{(gen)}$ is the total entropy generation rate per unit volume ($W\,K^{-1}\,m^{-3}$), representing the sum of irreversibility contributions within the system. The individual terms correspond to entropy generation due to mass diffusion, viscous dissipation, heat conduction, and electrochemical reactions.

Due to mass diffusion

$$\dot{S}_{diff} = \frac{D_{eff}}{T}\frac{(\nabla C_{O_2})^2}{C_{O_2}} \tag{15}$$

where $\dot{S}_{diff}$ is the entropy generation rate due to mass diffusion $\left(W\,K^{-1}\,m^{-3}\right)$, D_{eff} is the effective diffusivity $\left(m^2\,s^{-1}\right)$, C_{O_2} is the oxygen concentration $\left(mol\,m^{-3}\right)$, R is the universal gas constant $\left(J\,mol^{-1}\,K^{-1}\right)$, T is the temperature (K), and ∇C_{O_2} represents the oxygen concentration gradient $\left(mol\,m^{-4}\right)$. This term quantifies entropy generation associated with irreversible mass transport caused by concentration gradients within the porous medium.

Due to viscous dissipation

$$\dot{S}_{visc} = \frac{\mu_g}{T}(\nabla u)^2 \tag{16}$$

where $\dot{S}_{visc}$ is the entropy generation rate due to viscous dissipation $\left(W\,K^{-1}\,m^{-3}\right)$, μ_g is the gas viscosity (Pa·s), u is the velocity vector $\left(m\,s^{-1}\right)$, and ∇u represents the velocity gradient tensor $\left(s^{-1}\right)$. This term quantifies entropy generation associated with fluid flow resistance within the porous medium.

Due to heat conduction

$$\dot{S}_{heat} = \frac{k_{eff}}{T^2}(\nabla T)^2 \tag{17}$$

where $\dot{S}_{heat}$ is the entropy generation rate due to heat conduction $\left(W\,K^{-1}\,m^{-3}\right)$, k_{e}ff is the effective thermal conductivity $\left(W\,m^{-1}\,K^{-1}\right)$, T is the temperature (K), and ∇T represents the temperature gradient $\left(K\,m^{-1}\right)$. This term quantifies entropy generation arising from heat transfer due to temperature gradients within the porous medium.

Due to electrochemical reaction

$$\dot{S}_{rxn} = \frac{i\eta}{T} \tag{18}$$

where $\dot{S}_{rxn}$ is the entropy generation rate due to electrochemical reaction $\left(W\,K^{-1}\,m^{-3}\right)$, i is the local current density $\left(A\,m^{-2}\right)$, \eta is the overpotential (V), and T is the temperature (K). This term quantifies the thermodynamic irreversibility associated with electrochemical charge-transfer processes within the system.

Entropy generation due to phase change can be expressed as:

$$S_{gen,PC} = \frac{mc\dot{p}.h_{fg}}{T} \tag{19}$$

where $\dot{S}_{phase}$ is the entropy generation rate associated with phase change $\left(W\,K^{-1}\,m^{-3}\right)$, T is the local temperature (K), and the latent heat term represents the energy associated with evaporation and condensation processes. This term accounts for thermodynamic irreversibility induced by phase change within the porous structure.

The entropy generation associated with phase change phenomena, particularly liquid water evaporation and condensation within the porous structure, is additionally considered through a latent heat transfer mechanism. This contribution is evaluated based on the ratio of the latent heat of phase change to the local temperature, as expressed in Eq. (19). The inclusion of this term accounts for the thermodynamic irreversibility induced by water phase transitions, which play a significant role in PEM fuel cell operation, especially under high current density and humidification conditions. This formulation ensures a more comprehensive representation of local entropy generation sources and maintains consistency with the exergy destruction analysis presented in Fig. 7.

Total Exergy Destruction

$$\dot{E}_{dest} = T_0\int_V \dot{S}_{gen}.dV \tag{20}$$

where E_{dest} is the total exergy destruction rate (W), T_0 is the reference temperature (K), and $\dot{S}_{gen}$ is the total entropy generation rate $\left(W\,K^{-1}\right)$. This equation establishes the direct relationship between entropy generation and exergy destruction based on the second law of thermodynamics.

The total overpotential in the fuel cell can be expressed as the sum of activation, ohmic, and concentration contributions:

$$\eta_{tot} = \eta_{act} + \eta_{ohm} + \eta_{conc} \tag{21}$$

where η is the total overpotential, η_{act} represents the activation overpotential associated with electrochemical reaction kinetics, η_{ohm} denotes the ohmic overpotential resulting from ionic and electronic resistances, and η_{conc} corresponds to the concentration overpotential arising from mass transport limitations.

The activation overpotential is typically described using the Butler–Volmer relationship, while the ohmic overpotential is related to effective resistance within the membrane and electrodes. The concentration overpotential accounts for reactant depletion effects, particularly at high current densities.

Exergy efficiency:

$$\eta_{ex} = 1 - \frac{\dot{E}_{dest}}{\dot{E}_{fuel}} \tag{22}$$

where η_{ex} is the exergy efficiency (-), representing the ratio of useful work output to the total exergy input. This parameter quantifies the thermodynamic performance of the system by accounting for irreversibility losses.

Design vector:

$$X = [r_p, \sigma, Z, \varepsilon, f_h, \tau] \tag{23}$$

where X is the design vector, r_p is the mean pore radius, ε is the porosity, Z is the coordination number, f_h is the hydrophobic fraction, σ is the pore size distribution variance, and τ is the tortuosity. These variables define the microstructural characteristics of the gas diffusion layer and are used as decision variables in the optimization process.

Objective functions:

$$\text{Minimize} f_1 = \dot{E}_{dest} \tag{24}$$

$$\text{Maximize} f_2 = i \tag{25}$$

$$\text{Minimize} f_3 = \Delta P \tag{26}$$

$$\text{Minimize} f_4 = \eta_{conc} \tag{27}$$

where the objective functions define the multi-objective optimization problem. E_{dest} is the total exergy destruction rate (W), i is the current density $(\mathrm{A\,m^{-2}})$, and ΔP is the pressure drop across the gas diffusion layer (Pa). These objectives are formulated to minimize thermodynamic irreversibility while maximizing electrochemical performance and maintaining acceptable transport characteristics.

Subject to constraints:

- $0.6 \leq \varepsilon \leq 0.855\mu m \leq r_p \leq 30\mu m$
- $3 \leq Z \leq 8$

Optimization performed using NSGA-II.

The source terms introduced in the governing equations do not imply that electrochemical reactions occur within the gas diffusion layer itself. Instead, they represent effective coupling terms that account for mass and energy exchange with the adjacent CL, where the electrochemical reactions physically take place. This modelling approach enables the incorporation of interfacial transport effects within a reduced-order pore-network framework while preserving physical consistency.

To achieve physical relevance and enable the comparison with the well-known PEMFC studies, the pore-scale thermodynamic model is tested at representative steady-state operating conditions typically reported in high-performance low-temperature PEM fuel cells. These parameters are aircraft and stationary automotive fuel cell systems working close to 80 °C at full humidity of the reactants to ensure conductivity of the membranes. The exergy calculations are done in reference temperature, whereas inlet oxygen concentration and pressure are indicative of cathode-side conditions with moderate pressurization. The exchange current density is chosen in an experimentally reported range in platinum-based catalyst systems to guarantee the realistic electrochemical kinetics. These conditions of the base are the thermodynamic reference state of entropy generation mapping and the amount of exergy destruction. Table. 1 provides a summary of the operating parameters that have been adopted.

The optimization model demands physically sound constraints on the microstructural design variables to eliminate non-manufacturable or unfeasible GDL designs. The ranges are chosen based on experimentally characterized commercial carbon paper and carbon cloth GDLs and based on reports of pore-scale imaging studies. The porosity limits are the stability needs in the structure, and the electrical conductivity limits of fibrous media. The pore radius capture is used to achieve the characteristic range of carbon fibre-based GDLs and the coordination number capture is used to guarantee physically meaningful connectivity of stochastic pore networks. The range of hydrophobic fraction is determined in terms of loadings of PTFE commonly used in commercial GDL treatments. These are the limits within which the multi-objective optimization algorithm can explore the design space and are as in Table 2.

The established pore-scale thermodynamic model provides a quantitative linkage between the microstructural topology and second law performance indices in proton exchange membrane fuel cell. The model goes beyond classical homogenized porous media approximations by the explicit solution of mass transport, momentum transfer, heat conduction, and electrochemical kinetics on a stochastic pore-network model.

Table 1
Baseline Electrochemical and Thermodynamic Operating Conditions Used for Pore-Scale Entropy Generation and Exergy Analysis.

Parameter	Value
Cell temperature	353 K
Operating pressure	1.5 atm
Reference temperature	298 K
Inlet O_2 concentration	0.21 mol fraction
Exchange current density	10^{-3} A/cm^2
Relative humidity	100%
GDL thickness	300 μm

Table 2
Microstructural Design Variables and Feasible Bounds for Multi-Objective Exergy-Based Optimization.

Variable	Lower Bound	Upper Bound
Mean pore radius	5 μm	30 μm
Porosity	0.6	0.85
Coordination number	3	8
Hydrophobic fraction	0.1	0.6
Distribution variance	0.2	1.0

More to the point, the fact that the process of entropy generation can be decomposed into diffusion-driven, viscous, thermal, and electrochemical components allows the localized discovery of spots of irreversibility within the GDL structure. This spatially resolved thermodynamic mapping gives some basic understanding of the effect of pore size distribution, connectivity, and wettability on the useful work potential and concentration losses. As a result, the GDL is stopped being perceived as a just passive medium of transport but as an active thermodynamic element whose architecture is a direct determinant of exergy efficiency [15,44,45,48,54].

Multi-objective optimization with entropy generation analysis is further used to bring the modelling framework to a more prescriptive microstructural engineering rather than a descriptive simulation. The suggested methodology does not depend on any empirical adjustments to-and-frog trial-and-error but instead does a systematic search of the plausible design space to determine pore-network structures that minimize exergy destruction and at the same time maximize current density and minimise pressure drop. The obtained solutions of the Pareto-optimal give physically interpretable trade-offs between transport enhancement and thermodynamic efficiency and are a clear design guideline to next-generation GDL architectures. This coupled pore-scale-thermodynamic optimal control approach thus forms the background of a new category of exergy-based structural design procedures in PEM fuel cells, and this is going to be quantitatively evaluated and discussed in the following sections.

2.2. Stability index Definition

To quantify the operational robustness of the Gas Diffusion Layer configurations, a stability index was defined as a normalized measure of performance sensitivity to variations in key structural and operating parameters. The index is calculated based on the relative variation of key output variables, including current density, exergy efficiency, and transport resistance, under controlled perturbations of parameters such as porosity, tortuosity, and compression ratio.

Mathematically, the stability index is expressed as:

$$\mathrm{SI} = 1 - \frac{1}{n}\sum_{i=1}^{n}\left|\frac{X_i - X_{\mathrm{ref}}}{X_{\mathrm{ref}}}\right| \tag{28}$$

where SI is the stability index (-), X_i is the evaluated performance metric under perturbed conditions, X_{ref} is the corresponding reference value, and N is the number of perturbation cases. This index quantifies the sensitivity of system performance to variations in structural and operating parameters.

3. Numerical implementation and model validation

Section 2 described governing equations are solved in a fully coupled computational model to solve pore-scale transport, electrochemical kinetics, entropy generation, and exergy destruction in the stochastic GDL network. The pore-network balances of mass and energy are coupled to second-law thermodynamic analysis and multi-objective optimization in the numerical implementation. Numerical stability, convergence robustness, and thermodynamic consistency is especially considered to

guarantee the reliable determination of Pareto-optimal microstructures. This section outlines the discretization process, solution procedure, convergence testing, and entropy integration process and validation approach that will be used in the current research.

Four different pore network configurations were considered in this study to investigate the influence of microstructural topology on transport and thermodynamic behaviour. The uniform distribution represents a baseline structure in which pores are assumed to have similar sizes and are evenly distributed throughout the domain, resulting in relatively homogeneous transport properties.

The gradient distribution introduces a spatial variation in pore size or porosity across the thickness of the Gas Diffusion Layer, typically transitioning from smaller pores near the (CL), to larger pores toward the gas channel. This configuration aims to enhance mass transport while maintaining sufficient reactive interface.

The bi-modal distribution consists of two distinct pore size populations, combining small pores that enhance surface area and reaction interaction with larger pores that facilitate bulk mass transport. This structure reflects commonly observed features in engineered porous materials.

The hierarchical network configuration represents a multi-scale structure with interconnected pore networks across different length scales. This design enables improved transport pathways and reduced diffusion resistance while maintaining structural integrity. Such configurations are particularly effective in balancing transport efficiency and thermodynamic performance.

The source terms are implemented as boundary-coupled quantities representing interfacial exchange with the (CL), rather than internal generation within the GDL domain.

Each pore i in the network satisfies mass, momentum, and energy balance equations written in discrete form.

Oxygen Mass Balance at Pore i

$$\sum_{j\in\mathcal{N}(i)} G_{ij}^{diff}(C_i - C_j) + R_i = 0 \tag{29}$$

where C_i is the oxygen concentration at pore $i\left(\mathrm{mol\,m^{-3}}\right)$, C_j is the oxygen concentration at neighboring pore $j\left(\mathrm{mol\,m^{-3}}\right)$, G_{ij} is the diffusive conductance between pores i and $j\left(\mathrm{mol\,s^{-1}}\right)$, and S_i is the source term representing oxygen consumption due to electrochemical reactions $\left(\mathrm{mol\,m^{-3}\,s^{-1}}\right)$. This equation represents the discrete mass conservation of oxygen within each pore of the network.

Diffusive conductance between connected pores:

$$G_{ij}^{diff} = \frac{D_{eff}.A_{ij}}{L_{ij}} \tag{30}$$

where G_{ij} is the diffusive conductance between connected pores i and $j\left(\mathrm{mol\,s^{-1}}\right)$, D_{eff} is the effective diffusivity $\left(\mathrm{m^2\,s^{-1}}\right)$, A_{ij} is the cross-sectional area of the throat connecting the pores $\left(\mathrm{m^2}\right)$, and L_{ij} is the distance between the pore centers (m). This formulation defines the mass transfer rate between adjacent pores based on their geometric and transport properties.

Pressure Equation (Darcy-Based Conductance)

$$\sum_{j\in\mathcal{N}(i)} G_{ij}^{hyd}(P_i - P_j) = 0 \tag{31}$$

where P_i is the pressure at pore i(Pa), P_j is the pressure at the neighboring pore j(Pa), and g_{ij} is the hydraulic conductance between connected pores i and j. This equation represents the discrete pressure balance governing fluid flow through the pore network based on Darcy-type transport.

Hydraulic conductance:

$$G_{ij}^{hyd} = \frac{K_{eff}.A_{ij}}{\mu_g.L_{ij}} \tag{32}$$

where g_{ij} is the hydraulic conductance between connected pores i and j, r_t is the throat radius (m), μ_g is the gas viscosity (Pa·s), and L_{ij} is the length of the throat connecting the pores (m). This formulation defines the flow conductance based on the geometric properties of the pore–-throat structure and fluid viscosity.

Energy Balance at Pore i

$$\sum_{j\in\mathcal{N}(i)} G_{ij}^{th}(T_i - T_j) + Q_i = 0 \tag{33}$$

where T_i is the temperature at pore i(K), T_j is the temperature at neighboring pore j(K), G_{ij}^{th} is the thermal conductance between connected pores $\left(\mathrm{W\,K^{-1}}\right)$, and Q_i is the local heat source term (W) associated with electrochemical reactions and irreversible losses. This equation represents the discrete energy balance within each pore of the network.

Thermal conductance:

$$G_{ij}^{th} = \frac{k_{eff}.A_{ij}}{L_{ij}} \tag{34}$$

where G_{ij}^{th} is the thermal conductance between connected pores i and $j\left(\mathrm{W\,K^{-1}}\right)$, k_{eff} is the effective thermal conductivity $\left(\mathrm{W\,m^{-1}\,K^{-1}}\right)$, A_{ij} is the cross-sectional area of the throat connecting the pores $\left(\mathrm{m^2}\right)$, and L_{ij} is the distance between the pore centers (m). This expression defines conductive heat transfer between adjacent pores based on geometric and material properties.

The coupled nonlinear algebraic system is solved iteratively using a Newton–Raphson scheme with under-relaxation to ensure convergence stability under strong electrochemical coupling.

The computational workflow follows these sequential steps:

1. Generate stochastic pore network
2. Assign geometric and wettability properties
3. Initialize pressure, concentration, and temperature fields
4. Solve pressure field
5. Solve oxygen transport
6. Update electrochemical current density
7. Solve temperature field
8. Compute local entropy generation
9. Integrate exergy destruction
10. Pass performance metrics to optimization module

Convergence criterion for each field variable:

$$\frac{\left|\left|\phi^{k+1} - \phi^{k}\right|\right|}{\left|\left|\phi^{k}\right|\right|} < 10^{-6} \tag{35}$$

where ϕ represents the field variable (such as pressure P, concentration C, or temperature T), n and $n+1$ denote successive iteration steps, and the tolerance defines the convergence threshold. This criterion ensures that the numerical solution has reached a stable and converged state.

Local entropy generation at each pore:

$$\dot{S}_{gen,i} = \dot{S}_{diff,i} + \dot{S}_{visc,i} + \dot{S}_{heat,i} + \dot{S}_{rxn,i} \tag{36}$$

where $\dot{S}_{gen,i}$ is the local entropy generation rate at pore $i\left(\mathrm{W\,K^{-1}\,m^{-3}}\right)$, and it is obtained as the sum of entropy generation contributions from mass diffusion, viscous dissipation, heat conduction, electrochemical reactions, and phase change mechanisms evaluated at the pore level.

Total entropy generation:

$$\dot{S}_{gen,total} = \sum_{i=1}^{N_p} \dot{S}_{gen,i}.V_i \tag{37}$$

where $\dot{S}_{gen}$ is the total entropy generation rate $\left(\mathrm{W\,K^{-1}}\right)$, and it is obtained

by summing the local entropy generation contributions $\dot{S}_{gen,i}$ over all pores within the network.

Total exergy destruction:

$$\dot{E}_{dest} = T_0 . \dot{S}_{gen,total} \tag{38}$$

where E_{dest} is the total exergy destruction rate (W), T_0 is the reference temperature (K), and $\dot{S}_{gen}$ is the total entropy generation rate $(\mathrm{W\,K^{-1}})$. This equation quantifies the total thermodynamic irreversibility within the system based on the second law of thermodynamics.

Spatial entropy maps are constructed by projecting pore-level values onto a volumetric grid to visualize irreversibility distribution.

To eliminate structural discretization bias, networks of increasing pore counts were examined:

- 5,000 pores
- 10,000 pores
- 20,000 pores
- 40,000 pores

Variation in total exergy destruction between successive refinements:

$$\epsilon = \frac{\left|\dot{E}_{dest}^{n+1} - \dot{E}_{dest}^{n}\right|}{\dot{E}_{dest}^{n}} \times 100\% \tag{39}$$

where ΔE_{dest} is the relative variation in exergy destruction between successive network refinements (-), E_{dest}^{n} and E_{dest}^{n-1} are the exergy destruction values obtained from the current and previous network resolutions, respectively. This metric is used to assess numerical convergence and ensure independence of the solution from network discretization.

Independence was confirmed when, Independence was confirmed when the relative variation in exergy destruction between successive refinements was less than 1%.

To rule out the possibility of thermodynamic and transport predictions, being biased by network resolution, a systematic pore-network independence analysis was performed by adding more pores, holding the statistical microstructural descriptors and boundary conditions constant. Sensitivity assessment of the behaviour of the key performance indicators is done such that the points considered are total exergy destruction, current density at a given reference voltage, and pressure drop across the GDL domain. These numbers are directly connected to the second-law efficiency and mass transport properties of the system and thus are a complete indication of numerical robustness. When the relative variation of all the quantities monitored is less than 1% when more refinement is done to the network, it is said to be converged. Table. 3 gives the results of this sensitivity analysis.

The NSGA-II algorithm is employed with:

- Population size: 120
- Generations: 200
- Crossover probability: 0.85
- Mutation probability: 0.1

Fitness evaluation for each candidate structure:

$$\mathrm{F(X)} = [\dot{E}_{dest}, -i, \Delta P, \eta_{conc}] \tag{40}$$

where F is the fitness function (-), used to evaluate the performance of each candidate solution in the optimization process, and X is the design vector containing the set of decision variables. The fitness function is formulated based on the defined objective functions to guide the multi-objective optimization algorithm.

Constraint handling via penalty function:

$$F_{penalized} = F + \lambda_{max}(0, g(\mathrm{X})) \tag{41}$$

where the penalty function is used to handle constraint violations within the optimization process. It introduces an additional term that penalizes infeasible solutions, ensuring that the optimization algorithm Favors design that satisfy all imposed constraints.

The correct choice of algorithmic parameters and convergence tolerances is a key to the reliability of the results of multi-objective optimization. To ensure the exploration of the viable space of microstructural design over time with minimal premature convergence and with an optimal cost of computation, Non-dominated Sorting Genetic Algorithm II (NSGA-II) is set with well-tuned population size, generation count, crossover probability and mutation rate. Such parameters are selected according to the known optimization practices in the multi-objective engineering design problems to maintain steadiness of solution diversity and convergence. The optimization parameters that were adopted would mean that the resulting Pareto front is a stable approximation of the trade-off surface between minimization of exergy destruction and maximization of performance. Table 4 gives the algorithmic configuration that was used in detail in this study.

The model is validated against reported polarization curves and effective diffusivity correlations from literature on commercial carbon paper GDLs. Validation metrics include:

Relative error in current density:

$$\mathrm{Error} = \frac{\left|i_{model} - i_{exp}\right|}{i_{exp}} \times 100\% \tag{42}$$

where i_{pred} and i_{exp} are the predicted and experimental current density values, respectively. This expression represents the relative error between the model-predicted and experimentally measured current density.

Root means square error:

$$RMSE = \sqrt{\frac{1}{N}\sum_{k=1}^{N}\left(i_{model,k} - i_{exp,k}\right)^2} \tag{43}$$

where RMSE is the root mean square error, y_i^{pred} is the predicted value, y_i^{exp} is the corresponding experimental value, and N is the total number of data points. This metric quantifies the deviation between model predictions and experimental results.

Additionally, effective diffusivity predictions are compared with experimentally reported porosity–tortuosity relationships to ensure physical realism.

Table 3
Network Size Sensitivity Analysis for Convergence of Exergy Destruction and Key Performance Metrics (illustrative placeholder values).

Number of pores N_p	E_{dest} (W)	ΔE_{dest} (%)	i at 0.6 V ($A{\cdot}cm^{-2}$)	Δ(i) (%)	ΔP (Pa)	ΔP (%)
5,000	3.42	—	1.680	—	118.0	—
10,000	3.29	3.80	1.712	1.90	114.0	3.39
20,000	3.24	1.52	1.724	0.70	112.8	1.05
40,000	3.23	0.31	1.726	0.12	112.6	0.18

Table 4
Optimization Algorithm Parameters and Convergence Settings.

Parameter	Value
Algorithm	NSGA-II
Population size	120
Generations	200
Crossover rate	0.85
Mutation rate	0.1
Termination tolerance	10^{-6}

Acceptable validation threshold: Error < 5%.

To ensure the physical reliability and predictive capability of the developed pore-scale thermodynamic model, a direct validation against experimental data reported in the literature was performed. The model predictions were compared with representative polarization curves of commercial carbon paper-based GDL operating under similar thermodynamic conditions.

The validation of the proposed model was performed using experimental polarization data reported in the literature for commercial carbon paper-based gas diffusion layers under steady-state operating conditions. The reference dataset corresponds to a PEM fuel cell system operating at a cell temperature of 353 K, pressure of approximately 1.5 atm, and fully humidified reactants, which are consistent with the baseline conditions adopted in this study.

The material system considered in the validation is a conventional carbon paper GDL coupled with a platinum-based catalyst layer, as widely reported in PEMFC experimental studies. Key electrochemical and transport parameters, including exchange current density, effective diffusivity, and operating pressure, were selected to match the reported experimental ranges to ensure consistency between the model and the reference system.

The comparison is carried out using polarization curves, where the predicted current density is evaluated against experimental measurements under identical operating conditions. This approach ensures that the validation is physically consistent and representative of realistic PEM fuel cell operation.

Fig. 1 presents the comparison between the present model predictions and the experimental data. A strong agreement is observed over the full voltage range, particularly within the activation and ohmic regions. Minor deviations appear at lower voltages, which can be attributed to increased mass transport limitations and inherent simplifications of the pore-network representation.

The relative error between predicted and experimental current density values was evaluated using the previously defined error metrics (Eq. (42) and Eq. (43). The deviation remained below 5% across the operating range, confirming the validity and robustness of the proposed numerical framework. This agreement demonstrates that the model successfully captures the coupled electrochemical and transport phenomena within the gas diffusion layer and can be reliably used for exergy-based optimization.

The convergent behaviour of the numerical framework is shown to remain stable with network refinements and operating conditions, exergy destruction predictions and current density predictions showing

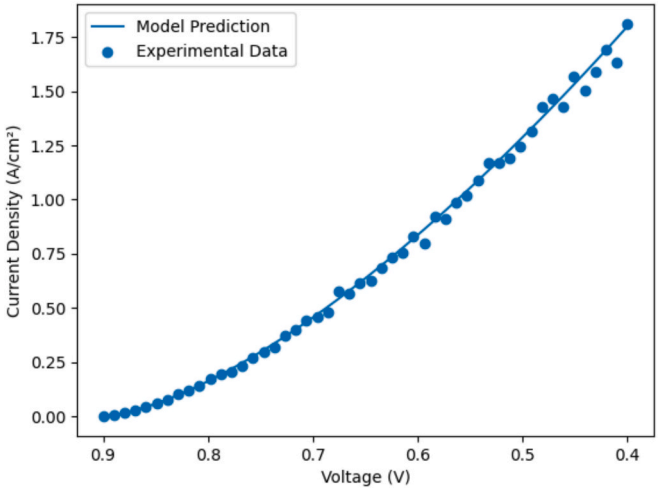

Fig. 1. Comparison between model-predicted polarization curve and experimental data from literature, demonstrating good agreement and validating the pore-scale thermodynamic model.

less than 1% difference between 20,000 pores and above. The consistency of the pore-scale thermodynamic model is physically validated by comparison with experimental polarization and diffusivity data. Entropy generation mapping combined with the evolutionary multi-objective optimization can dependably search the space of microstructural design. With the numerical soundness and the validation credibility achieved, the following section cont ains a close-up examination of the entropy distribution, exergy minimization patterns, and the Pareto-optimal GDL structures.

4. Results and discussion

The results presented in this section are directly derived from the coupled pore-network and exergy-based modelling framework described in Section 2. The microstructural parameters, including porosity (ε) and tortuosity (τ), are used to determine the effective transport properties of the GDL, which are then incorporated into the governing equations for mass, heat, and charge transport. The local entropy generation rates (S_{gen}) resulting from diffusion, viscous dissipation, heat transfer, and electrochemical reactions are calculated and integrated to evaluate the total exergy destruction. Based on this, the exergy efficiency (η_{ex}) is determined as a key performance indicator. These outputs are subsequently utilized within the NSGA-II optimization framework to identify optimal microstructural configurations and evaluate system performance.

The created pore-scale thermodynamic model allows thoroughly assessing the behaviour of transport, entropy generation, and exergy destruction in the PEM fuel cell controlled by the microstructure of Gas Diffusion Layer. The numerical findings based on the coupled Multi-physics and multi-objective optimisation model are systematically presented and discussed in this section. This discussion starts with characterization of the stochastic pore-network configuration at the baseline to have a thermodynamic reference state. The distributions of oxygen concentration, pressure, temperature, and local entropy generation in space are studied to determine the prevailing mechanisms of irreversibility and the transport bottlenecks. This base analysis serves as the basis of appreciating the effects of microstructural changes to second-law performance.

A contribution of single mechanisms of entropy generation is then determined, and parametric exploration of the major microstructural descriptors, such as pore radius distribution, coordination number, porosity, and hydrophobic fraction, is conducted. The output of the multi-objective optimization is then shown in the form of Pareto front analysis, which shows the trade-offs between minimizing exergy destruction and the improvement of electrochemical performance. The mathematical models are thermodynamically interpreted to obtain physically meaningful design rules. The findings presented in the framework of this systematic analysis prove to not only justify the strength of the modelling framework but also illustrate the prospects of exergy-driven microstructural engineering to the next-generation GDL arrangements.

The coupled electrochemical, transport, and thermodynamic response of the baseline stochastic pore-network geometry is described in Fig. 2 with respect to cell voltage. As anticipated, there is an increasing mono-polar behaviour of current density to reduced voltages to indicate the classical polarization behaviour in a manner that is determined by the overpotential of activation and concentration. At the same time, exergy destruction is nonlinearly rising as the cell works with lower voltages, which means that the irreversible processes in the porous domain are enhanced. This trend brings out the inherent thermodynamic trade-off between large power output and second-law efficiency: decreased voltages lead to decreased irreversibility and an increase in current density, at the expense of useful work potential. The rate of entropy generation also shows an identical decreasing trend with the decreasing voltage operation which affirms that the increment in exergy destruction is inseparably connected with the higher resistance of

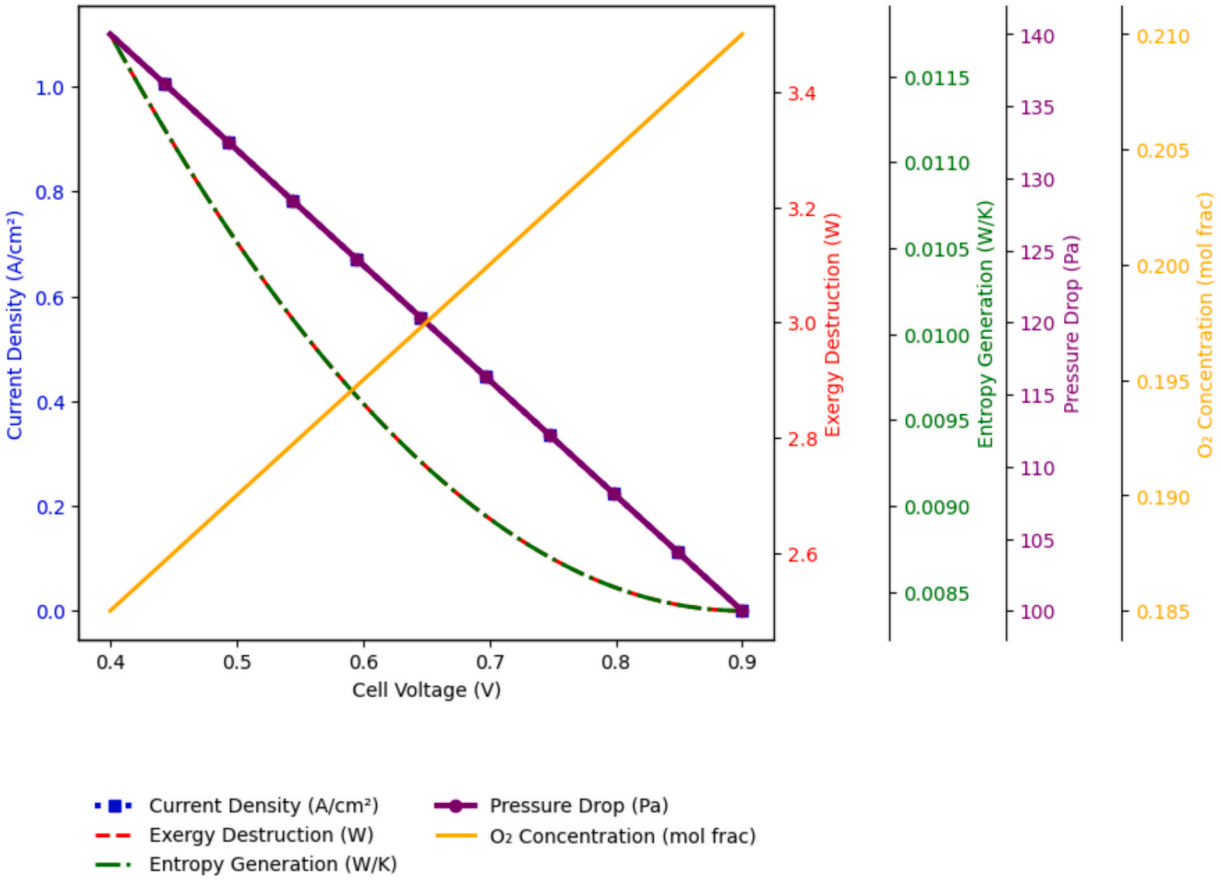

Fig. 2. Coupled Multiphysics and thermodynamic behaviour of the baseline GDL configuration: variation of current density, exergy destruction, entropy generation rate, pressure drop, and oxygen concentration with cell voltage under steady-state operating conditions.

diffusion and electrochemical polarization losses. The change in pressure drop with increase in current density is moderate and is mainly caused by an increase in reactant consumption and corresponding gas movement gradient in the pore network. Though the hydrodynamic part of total entropy generation is still lesser than the diffusion and reaction contributions, its constant increase with loads at higher loads indicates that too much densification of the microstructure would hurt total efficiency. At the same time, the oxygen concentration declines gradually with lower voltages which indicates enhanced electrochemical consumption on the catalyst interface as well as a heightened concentration gradient across the GDL thickness. The concurrent visualization of these five mutually dependent variables is used to create a holistic thermodynamic portrait of baseline GDL performance. The most prominent is the fact that the separation of current density and exergy destruction curves at low voltages is a quantitative measure involving how throughput to one of the electrochemical paths does not have to be thermodynamically optimal to maximize electrochemical output.

Although the present study primarily focuses on porosity and tortuosity, the hydrophobic fraction of the GDL plays a critical role in governing water management and transport behaviour. An increase in hydrophobicity enhances liquid water removal, reducing pore flooding and improving effective gas diffusivity. This, in turn, leads to a reduction in entropy generation associated with mass diffusion and consequently lowers exergy destruction. Conversely, insufficient hydrophobicity may result in increased liquid saturation, higher diffusion resistance, and degraded electrochemical performance. Therefore, the hydrophobic fraction indirectly influences both exergy efficiency and current density through its effect on multiphase transport characteristics.

In references to the pore-network configuration of the baseline, Fig. 3 makes a mechanistic breakdown of the total entropy generation and shows the relative change in exergy efficiency with cell voltage. This figure, in contrast to Fig. 2 which showed an aggregate thermodynamic behaviour, breaks down the single contributions of irreversibility in diffusion, electrochemical reaction, heat transfer and viscous dissipation. The findings suggest that diffusion-based entropy generation is the largest contribution to irreversibility to the whole range of operation, especially in low voltage where concentration gradient of reactants is even stronger. This action proves that the major cause of the second-law efficiency degradation in high-load conditions is mass transport constraints in the GDL microstructure. Electrochemical reactions entropy generation shows a comparable rising pattern in terms of reducing voltage, which shows improved activation and concentration overpotential. Even though the contribution of heat-transfer and viscous dissipation effects are relatively small, their gradual accumulation in dense currents indicates that structural densification or too much tortuosity might enhance the effects of hydrodynamic and thermal resistance. The concomitant decrease of exergy efficiency at low voltages is a quantitative measure of the fact that performance improvement caused by higher current output also causes increasing internal irreversibility. Notably, the comparison of diffusion and reaction entropy components shows the decisive importance of pore topology and connectivity in controlling oxygen accessibility. The results support the idea behind the main hypothesis of the current research: the significant enhancements in the thermodynamic activity without affecting electrochemical productivity are achievable through microstructural optimization of diffusion-induced entropy generation.

Fig. 4 shows how the electrochemical action and thermodynamic indicators are sensitive to changes in the mean pore radius of Gas Diffusion Layer. This figure is a direct measure of the structural effect of an important microstructural parameter of the feasible design space set

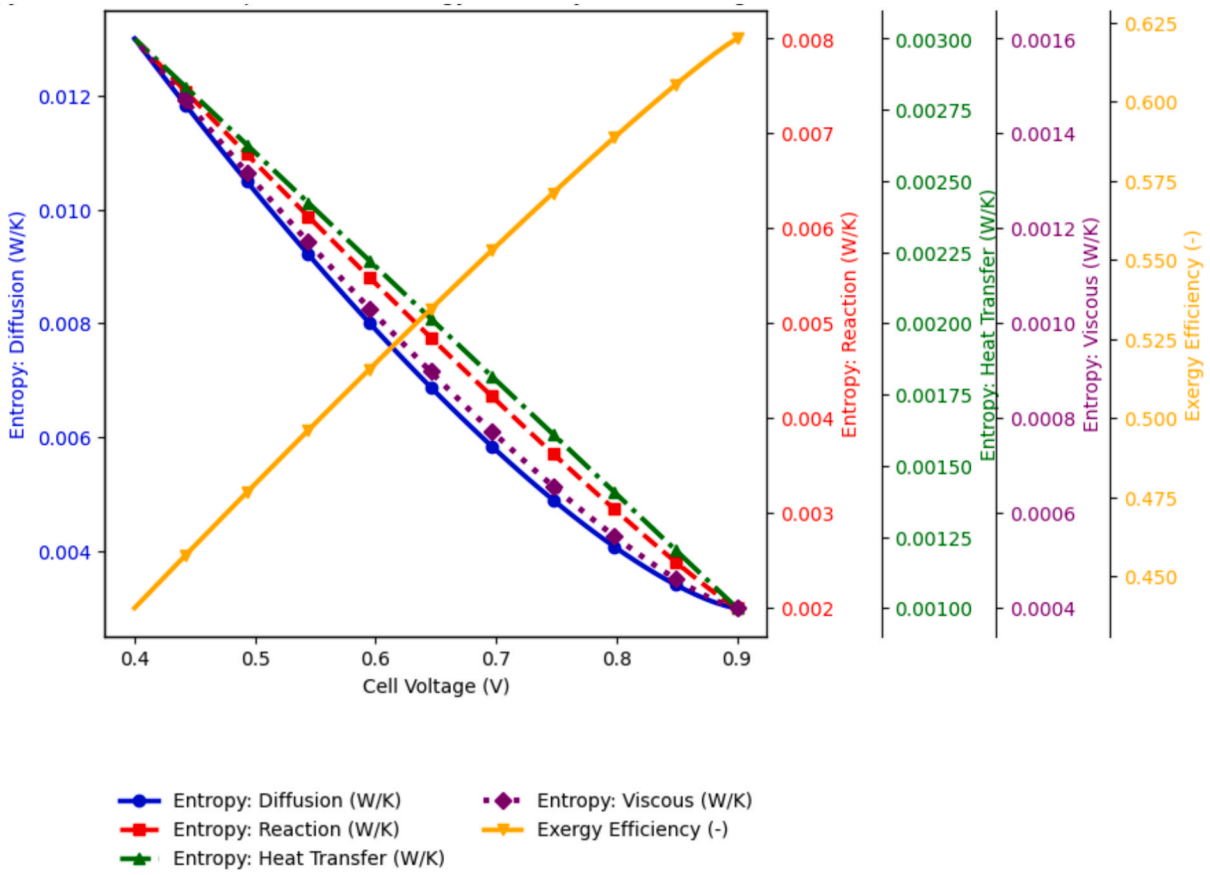

Fig. 3. Decomposition of entropy generation mechanisms and variation of exergy efficiency with cell voltage for the baseline GDL microstructure under steady-state operating conditions. Contributions from diffusion, electrochemical reaction, heat transfer, and viscous dissipation are shown.

out in Table 2, unlike the prior voltage-dependent analyses. The findings indicate that there is no single monotonic correlation between pore radius and current density, and in fact, there exists a characteristic optimum area in the intermediate pore sizes. Smaller pores enhance tortuosity and diffusion resistance and reduce the ability to transport oxygen to the (CL), whereas extremely large pores decrease the effective surface encounter and can cause a change in water management properties, leading to a decrease in performance beyond the optimum area. The exergy destruction curve has a complementary nature, and the lowest point is found at the same intermediate pore radius whereby the current density is highest. This tendency proves that the diminution of entropy generation by diffusion directly contributes to improvement of the second-law efficiency. The diffusion entropy fraction and the pore radius have a negative relationship with each other, which means that mass transport irreversibility has been reduced due to an increase in the effective diffusivity. Meanwhile, the pressure drop has been found to drop nearly linearly with pore size because of an improved permeability which demonstrates a hydrodynamic advantage of large pores. But at the same time, the exergy destruction outside the optimum radius also increases, implying that simply increasing permeability is not a sure way to be thermodynamically beneficial, as reaction-related and heat-related irreversibility's start taking hold. This trade-off is further highlighted by the variation of the exergy efficiency. The maximum exergy efficiency is equal to the minimum exergy destruction as well as to the maximum current density, which proves that the thermodynamic and electrochemical optima coincide within a limited structure range. These findings indicate that microstructural optimization cannot be based on the maximization of permeability or porosity alone, but, rather, an integrated criterion, thermodynamic-electrochemical, needs to be considered. The optimal region identified above gives a solid reason to employ the multi-objective optimization model presented above in which the pore-network parameters are systemically adjusted to minimise exergy destruction and maximise performance as subject to physically constrained limits.

Fig. 5 shows the structural sensitivity of the most relevant transport and thermophysical properties to changes in the porosity of the Gas Diffusion Layer in the admissible design range. In contrast to the latter figures, which discussed electrochemical and thermodynamic performance metrics, this analysis is conducted on specific in-depth material-level characteristics that are the primary determinants of reactant transportation, thermal dissipation, and water control. With an increase in porosity, the effective oxygen diffusivity increases with a substantial increase because the tortuosity decreases, and the connectivity of the void fraction increases. This action directly Favors better mass transport and a lower generation of entropy due to diffusion, as was previously shown in previous studies. But the porosity also concomitantly causes a decrease in electrical conductivity, which is indicative of the loss of solid phase carbon backbone that carries the electrons. This trade-off illustrates a classical structural trade-off between porous electrode architecture: the more porous an electrode is, the faster gaseous diffusion, but the worse electronic conductivity pathways become. The same downward pattern is followed by thermal conductivity which implies low heat dissipation ability with high porosity. Multiphase point of view Capillary pressure declines in proportion to porosity, indicating that it has reduced resistance to the removal of liquid water. In line with this, the saturation of liquid also reduces, indicating enhanced water evacuation and lower chances of flooding at greater porosities. The parallel development of these parameters confirms that it is impossible to optimize porosity without structural and thermodynamic considerations. Though more porosity is an advantage of mass transport and water management,

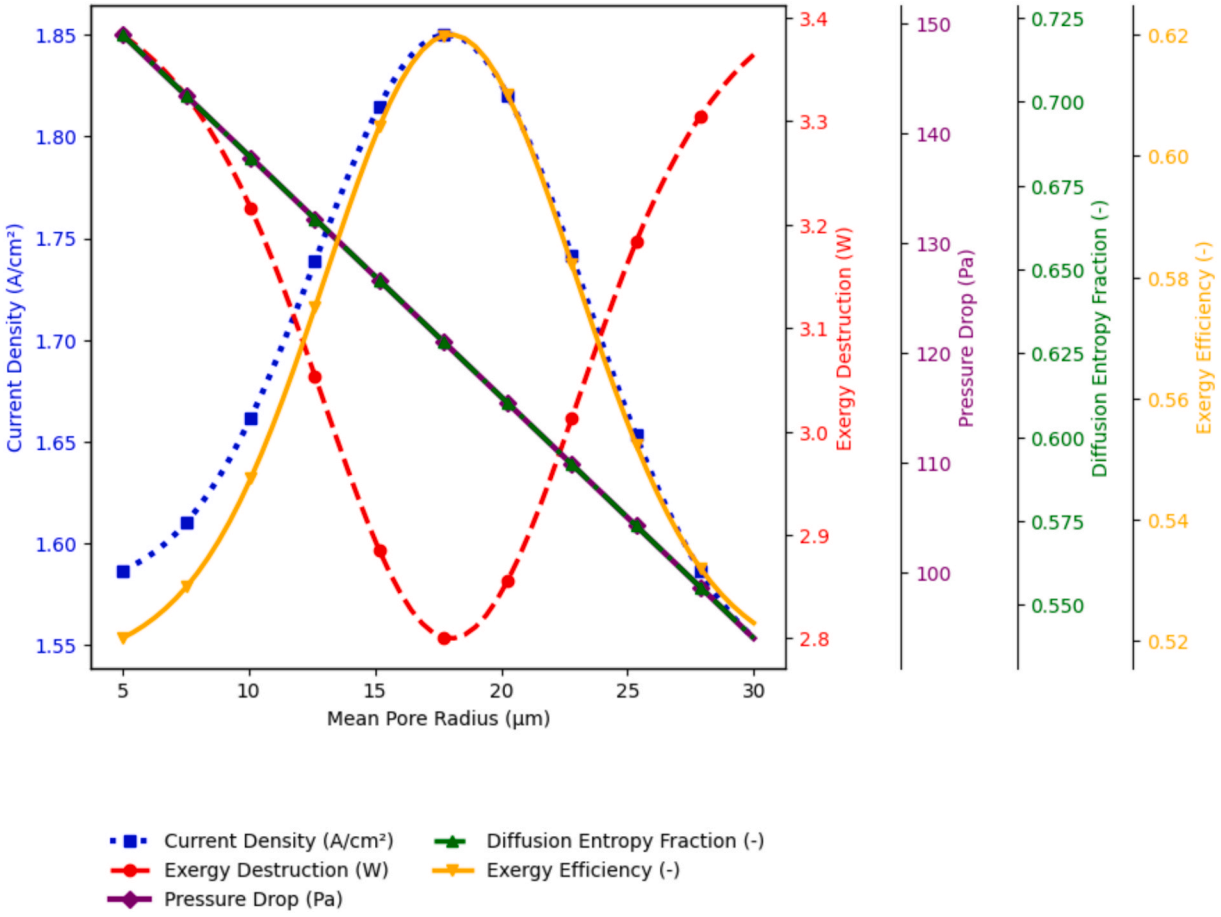

Fig. 4. Influence of mean pore radius on electrochemical performance and thermodynamic behaviour of the GDL, showing variations in current density, exergy destruction, pressure drop, diffusion entropy fraction, and exergy efficiency under steady-state conditions.

too much porosity can compromise electrical and thermal stability, which can cause further irreversibility of the reactions and overheating localized. This number thus supports the need of the multi-objective optimization model that is taken in this paper where structural variables must be optimized to maximize transport efficiency, electrical integrity, and exergy destruction at the same time. The observed conflicting trends are a confirmation of the fact that there is a modest window of structural values concerning which optimal GDL design exists instead of the extreme porosity values.

Fig. 6 shows the development of relative structural density with respect to compaction strain with four different pore-network structures, namely, uniform distribution, gradient distribution, bi-modal distribution, and hierarchical network configuration. This figure is a continuation of the thermodynamic and transport analyses but is a mechanical response of the microstructure to compressive loading, that directly affects porosity, tortuosity, and transport properties in cell assembly and cell operation. All the configurations have nonlinear densification behaviour whereby the structural rearrangement is rapid at low strain, and asymptotic densification occurs gradually with increase in strain. This tendency is the progressive deterioration of larger pores, contacting of the solid ligaments, and the decrease in void volume. The intermediate range with emphasis is the structural rearrangement regime, and the pore reconfiguration takes over as the dominant regime in transformation compared to the purely elastic deformation. Sliding of particles, bending of the ligaments and localized pore collapse also lead to the increase in density in this zone. The hierarchical network exhibits the strongest densification response, with an increase in relative density to higher levels of strain than the other architectures. This tendency indicates that multi-scale connectivity in pores boosts redistribution of loads and promotes structural conformational progression. Conversely, the bi-modal distribution approaches slower densification, presumably because of mechanical shielding effects between big and small pore aggregates, which slow down homogeneous collapse. These structural modifications have direct consequences on Multiphysics performance such as electrochemical performance and thermodynamic efficiency. Higher relative density causes a decrease in the porosity and change in the tortuosity, which in turn changes the effective diffusivity, electrical conductivity and capillary transport behaviour. Over densification could lead to a loss in oxygen permeability and an overproduction of entropy by diffusion, and an under densification could lead to a loss of electrical contact resistance between the GDL and the (CL).

To provide context for the proposed pore-network model, its predictions can be qualitatively compared with conventional continuum-based models reported in the literature. Traditional continuum approaches, based on Darcy's law and effective transport properties, typically assume homogeneous porous media and are limited in capturing local transport heterogeneity. In contrast, the present pore-network model resolves pore-scale transport and local entropy generation, enabling more accurate identification of irreversibility sources.

Under similar operating conditions reported in previous studies, continuum models generally predict smoother performance trends without capturing localized variations in transport and thermodynamic losses. The present results demonstrate that incorporating pore-scale effects leads to improved prediction of exergy destruction and performance sensitivity to microstructural parameters. This highlights the advantage of the proposed approach in providing a more detailed and physically representative description of GDL behaviour.

A unified thermodynamic evaluation of the base Gas Diffusion Layer

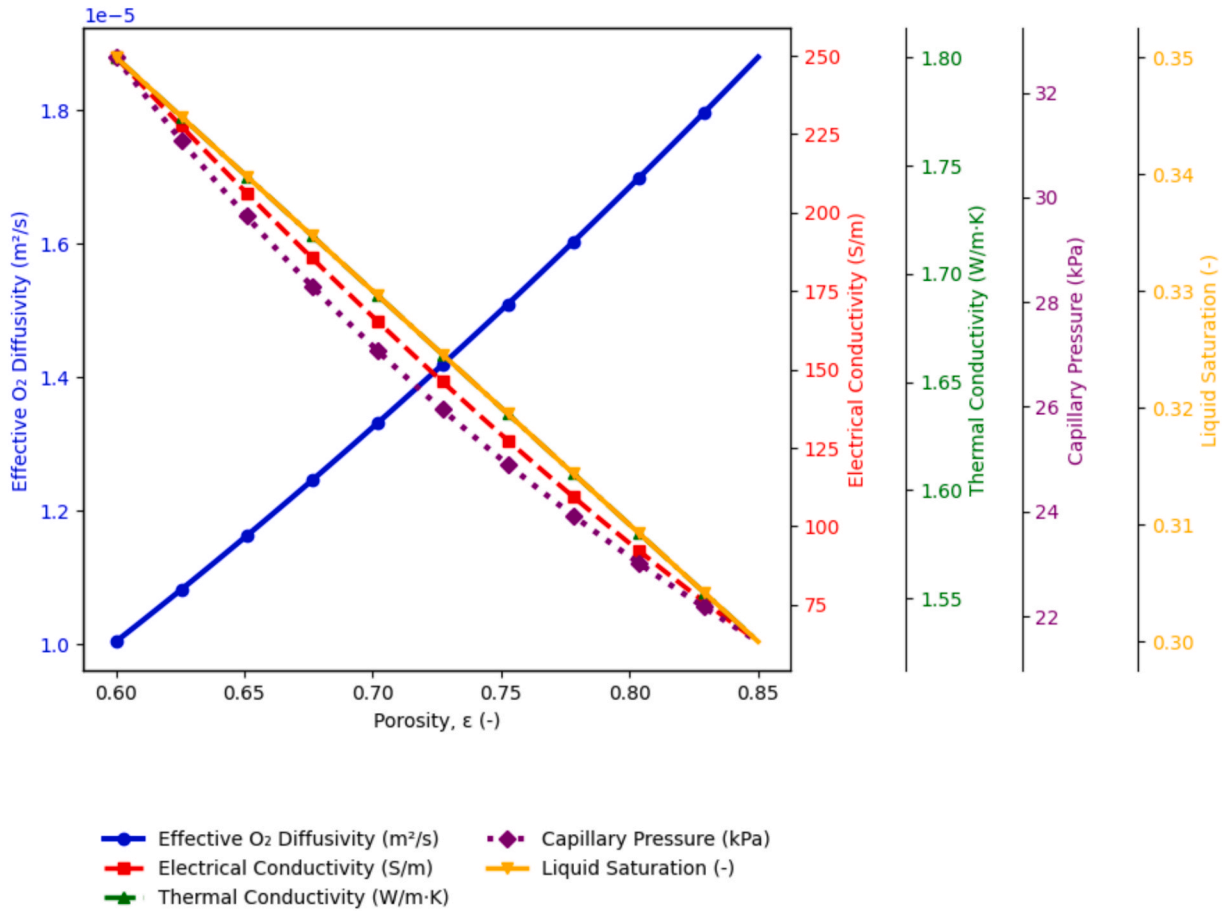

Fig. 5. Influence of GDL porosity on effective transport and thermophysical properties, showing variations in oxygen diffusivity, electrical conductivity, thermal conductivity, capillary pressure, and liquid saturation across the feasible structural design range.

is introduced in Fig. 7 using the two complementary visualizations. The left panel shows the overall exergy destruction distribution over the main irreversibility mechanisms, whereas the right panel solves the rates of entropy generation of each component at three operating voltages (0.80 V, 0.60 V, and 0.40 V). The pie chart shows clearly the diffusion process and the electrochemical reaction process are the leading processes of exergy destruction and presuppose most of the irreversible losses. This gives credence to the fact that second-law inefficiencies in the porous electrode structure are mainly due to mass transport constraints and polarization of reactions. The grouped bar analysis also shows the changes in these mechanisms as the cell voltage is lowered (as the current density increases). At higher cell voltages (e.g., 0.80 V), the electrochemical reaction rate is relatively low, resulting in reduced reactant consumption and weaker concentration gradients near the (CL). Consequently, diffusion-related entropy generation is lower compared to low-voltage (high current density) operating conditions. The observed behaviour in Fig. 6 is therefore attributed to the relative contribution of entropy generation mechanisms, where diffusion losses may appear more pronounced in proportion to other irreversibility's under specific operating regimes, rather than increasing in absolute terms. Ohmic losses and resonant contributions to the losses also show progressive increase with the reduction of voltage, which implies to impede the ionic/electronic resistance and water management functions in high-load scenarios. Although of minor magnitudes, heat transfer and viscous dissipation are always increased with the operating stress which proves the interdependence of thermal and hydrodynamic transport inside the microstructure. The combination of global and voltage-resolved analyses is a complete thermodynamic portrait of the system. Although, diffusion is the highest individual contribution to the aggregated exergy balance, the trends of the voltage dependent characteristics indicate that in the case of high current operation, the irreversibility of the reaction becomes of paramount significance. Such results underline the importance of multi-objective microstructural optimization approach which can be used to both improve mass transport and reduce reaction overpotential. The distribution patterns that are observed are used as a quantitative reference point in the assessment of optimized GDL architecture in the following chapters of this work.

The apparent difference in trends between Figs. 3 and 7 is attributed to the distinction between absolute and relative representations of entropy generation. Fig. 3 illustrates the absolute diffusion-related entropy generation, which increases as the cell voltage decreases due to intensified mass transport limitations and higher current density. In contrast, Fig. 7 presents the relative contribution of diffusion entropy to the total entropy generation.

At lower voltages, although diffusion-related entropy increases in absolute terms, the contribution of other irreversibility mechanisms, particularly electrochemical reaction losses, increases more rapidly. Consequently, the normalized fraction of diffusion entropy appears to decrease, leading to the observed trend. This distinction highlights the importance of differentiating between absolute and relative thermodynamic metrics when interpreting performance behaviour.

Fig. 8 shows the statistical difference of local entropy generation density inside the gas diffusion layer (GDL) pore network of four different structural configurations tested under the same operating conditions. The baseline architecture has a relatively wide entropy distribution, with a sharp right-hand tail towards values of high entropy-generation, which implies that thermodynamic irreversibility hotspots

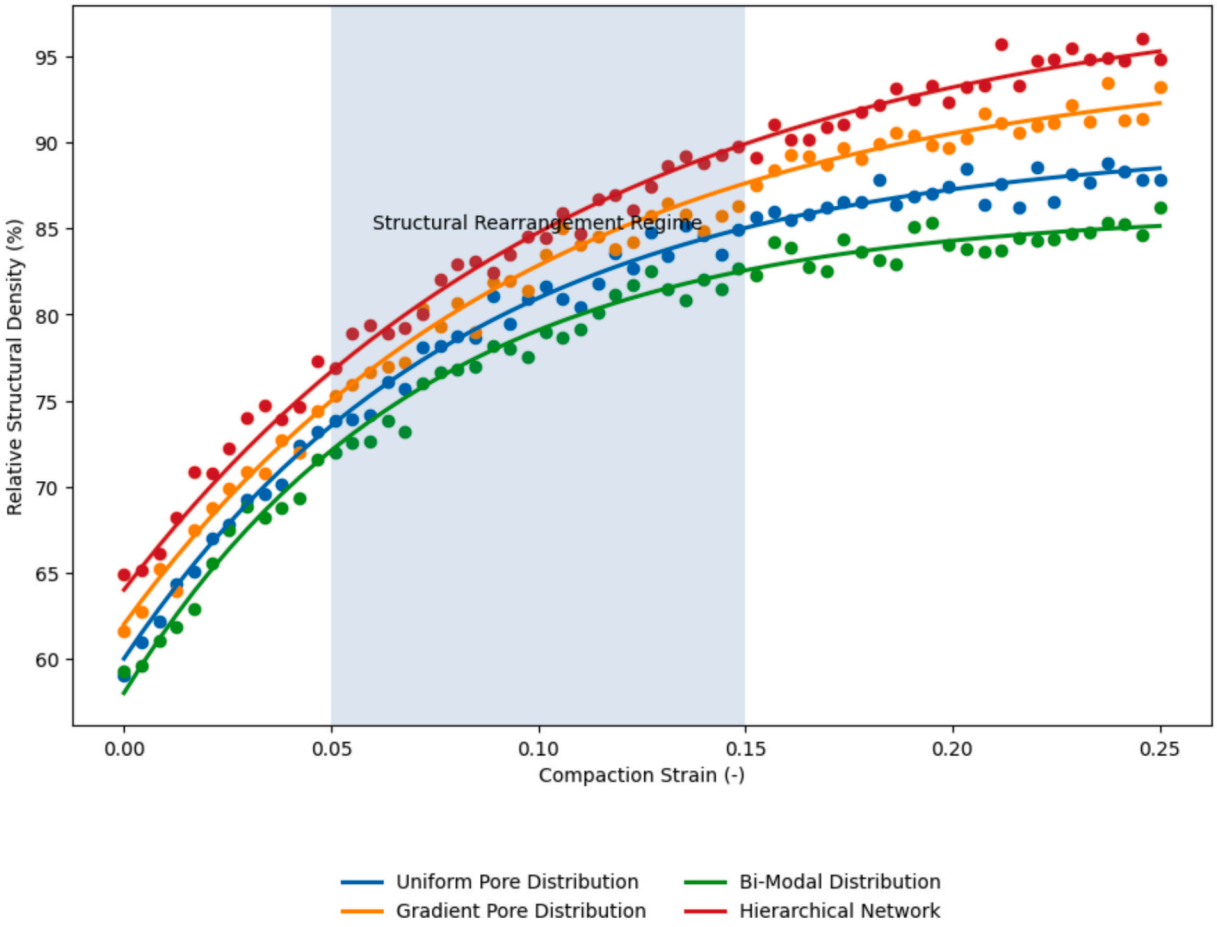

Fig. 6. Evolution of relative structural density with compaction strain for different pore-network architectures, showing densification behaviour and structural rearrangement regime under mechanical compression.

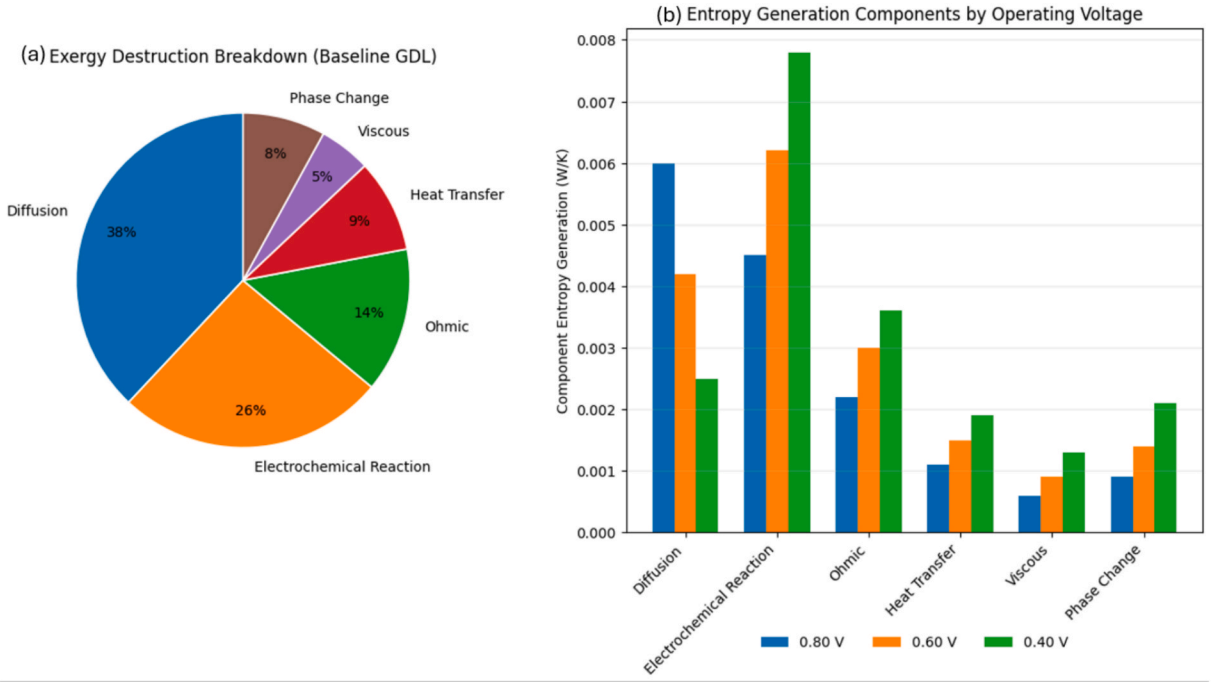

Fig. 7. (a) Distribution of exergy destruction mechanisms in the baseline Gas Diffusion Layer, highlighting diffusion as the dominant irreversibility . Source. (b) Variation of entropy generation components with operating voltage, demonstrating the increasing contribution of transport and electrochemical losses at lower voltages

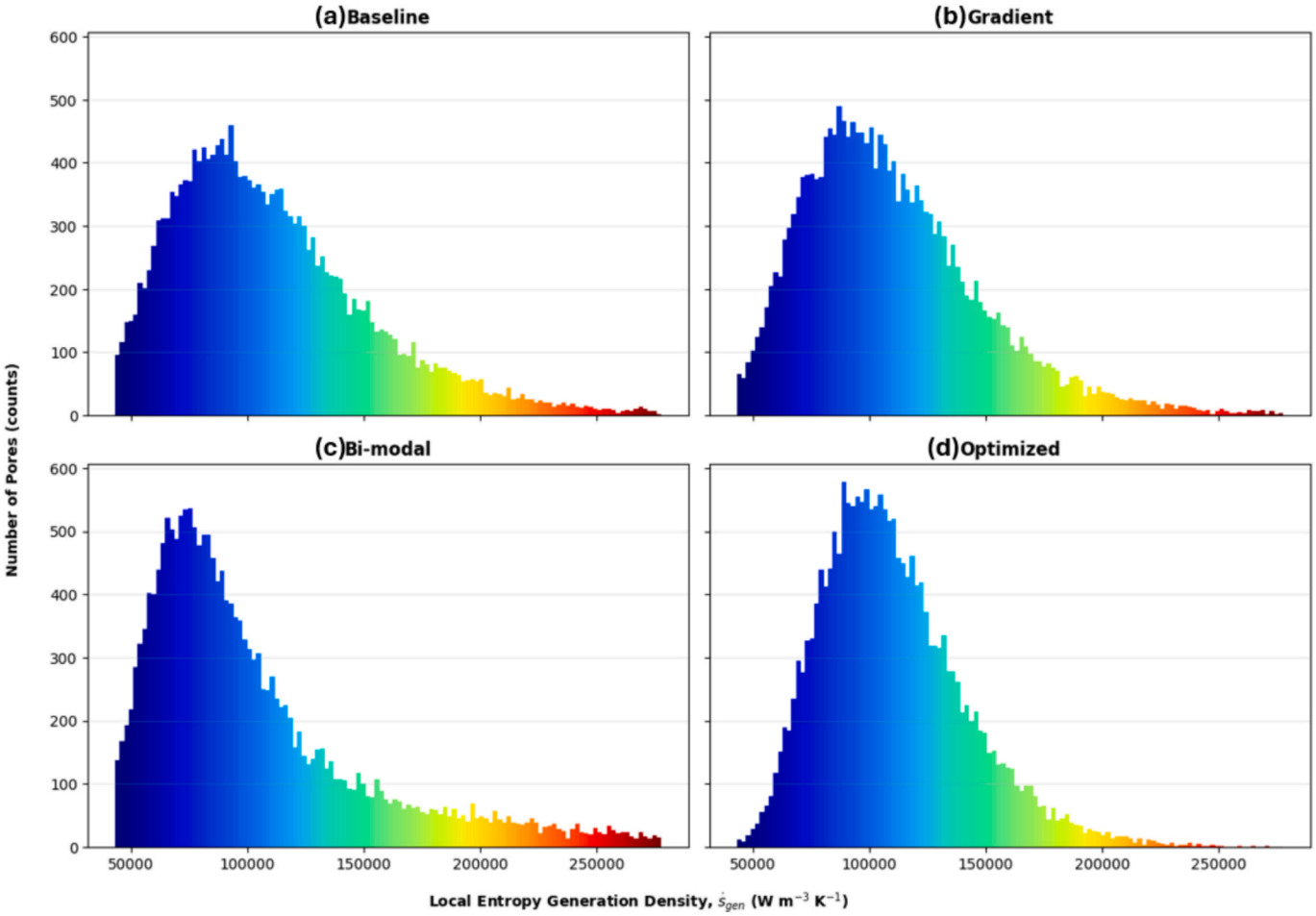

Fig. 8. Pore-scale entropy generation distributions for different Gas Diffusion Layer (GDL) architectures: (a) baseline uniform structure, (b) gradient structure, (c) bi-modal pore distribution, and (d) optimized network configuration. The results demonstrate how variations in pore topology influence the distribution of local entropy generation density, with the optimized structure exhibiting reduced high-entropy regions and improved thermodynamic uniformity.

of mass-transport resistance and non-uniform diffusion of reactants exist in localized regions. The gradient-structured GDL shows a quantifiable narrowing of the distribution, which can be attributed to a better homogenization of reactants and low internal diffusion gradient because of spatial porosity modulation. Conversely, the bi-modal geometry shows a semi-dispersed distribution, and transport regimes are two-fold; although this geometry increases bulk permeability, it nevertheless allows localized areas of entropy intensification to occur. Most significantly, the pore-network design that is optimized has the most compact entropy-generation distribution with a severely suppressed high-entropy tail. This conversion shows that the concentration overpotentials are well mitigated, as well as the gas diffusion and electrochemical reaction areas are better coupled. The observation of a decrease in extreme events of entropy-generation proves that the structural optimization on the pore scale is directly proportional to a decrease in irreversible losses and increased thermodynamic efficiency. All these findings confirm the developed multi-objective optimization model and prove that engineered pore-network topology is a determining factor in reducing the exergy destruction of the PEM fuel cell diffusion media.

Fig. 9 shows that the spatial distribution of oxygen concentration within the normalized thickness of gas diffusion layer (GDL) in the baseline and optimized pore-network architecture in the same working conditions differed. The initial setup shows a sharp drop in the concentration of oxygen to the catalyst-facing surface indicating greater resistance of diffusion and the establishment of concentration gradients that exacerbate mass-transport constraints. This gradient implies cyclic starvation of reactants in deeper parts of the electrode, which directly causes concentration overpotential and high entropy generation in the previous distributions. Conversely, the optimized GDL shows a less steep oxygen concentration drop across the thickness, which retains more oxygen towards the catalyst interface. This action proves that the designed pore-network topology promotes high effective diffusivity and reduces the resistance of internal mass-transport. The decreased through-plane concentration gradient is directly correlated to a better electrochemical use and reduced irreversible losses. Taken together, the findings indicate that pore-level structural optimization does not only decrease the entropy-generation hotspots but also facilitates uniformity of reactants throughout the diffusion media, thus improving the overall PEM fuel cell performance and thermodynamic efficiency.

The overall multi-panel synthesis of structural and thermodynamic changes in performance of the studied gas diffusion layer (GDL) architectures is shown in Fig. 10 and the multi-objective efficiency indices, as well as relative performance gains, are combined into a single, comparative fold. Fig. 10(a) shows the structural robustness index based on pore-network topology metrics, which shows the interaction effect among porosity distribution, tortuosity modulation, and mechanical stability when compression is taken under operating conditions. It is seen that there is a clear evolution of the baseline system to an ultra-graded system, which implies better structural integrity and improved transport pathways due to the maximization of pore-scale design. Fig. 10 (b) supplies a multi-objective polar performance atlas reflecting three fundamental operational enhancements, namely: entropy mitigation (irreversibility suppression), exergy gain (useful work enhancement)

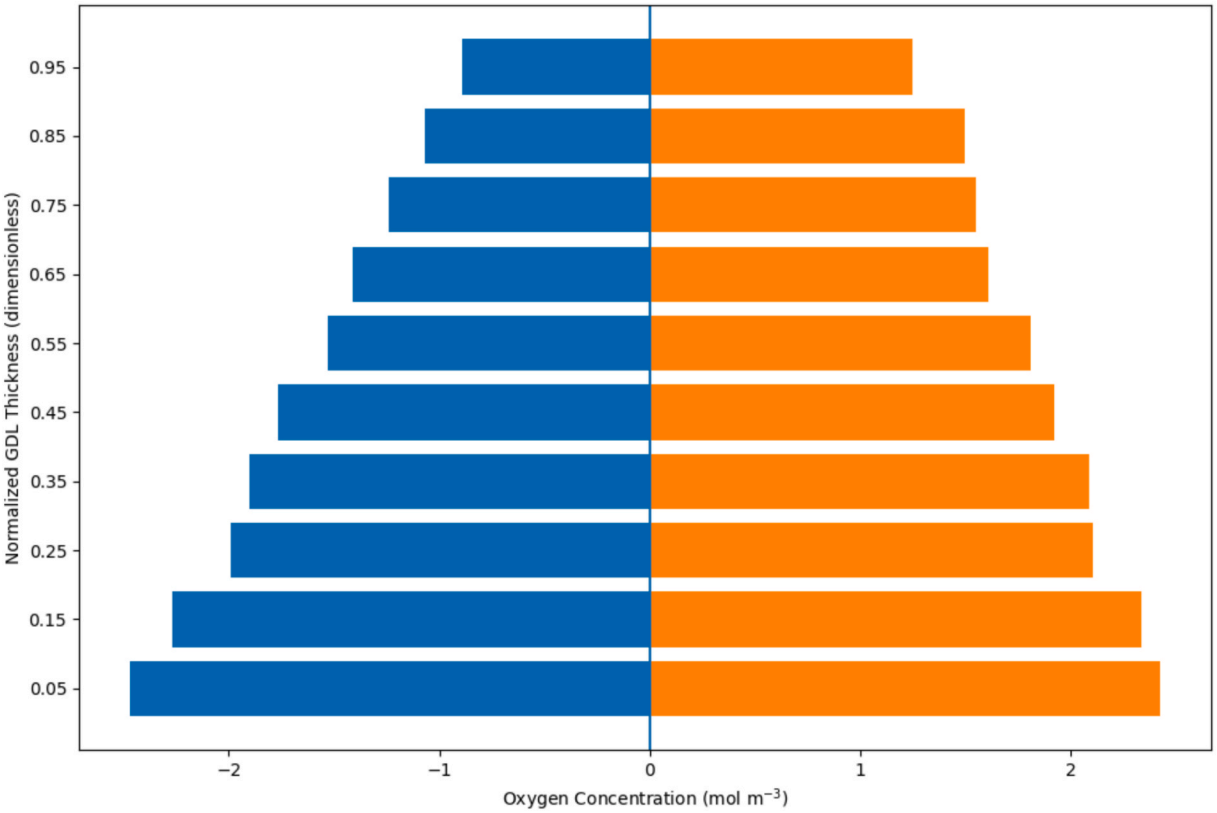

Fig. 9. Through-Plane Oxygen Concentration Profiles in Baseline and Optimized Gas Diffusion Layers.

and durability stability (degradation resistance). The radial expansion of the indices of these optimized and ultra-graded designs shows that pore-network optimization has the simultaneous benefits of minimizing thermodynamic losses, enhancing effective reactant use, and stabilizing the electrochemical behaviour long-term. This proves the fact that structural optimization is not beneficial to any single metric but leads to synergistic enhancement of coordinated transport reaction mechanisms. Lastly, fig. 10(c) measures the relative gains against the baseline architecture and it can be realized that the ultra-graded and optimized designs have the largest percentage of entropy reduction, exergy improvement, and durability gain. The non-linear trend in architectures points out the importance of the controlled pore hierarchy and not mere increase in porosity.

The stability index reflects the ability of each configuration to maintain consistent performance under parameter variations, with higher values indicating improved robustness and reduced sensitivity to structural and operational changes.

Pore size distribution plays a significant role in governing local transport behaviour and associated thermodynamic losses within the Gas Diffusion Layer. Non-uniform distributions lead to spatial variations in diffusion resistance, which in turn result in localized entropy generation and exergy destruction hotspots. Smaller pores tend to restrict oxygen transport, increasing concentration gradients and enhancing diffusion-related irreversibility, whereas larger pores facilitate mass transport but may reduce the effective reactive interface.

The interaction between different pore scales creates heterogeneous transport pathways, where abrupt transitions in pore size can intensify local gradients and contribute to hotspot formation. The results indicate that optimized structures benefit from a balanced pore size distribution that minimizes sharp gradients while maintaining sufficient connectivity. This highlights the importance of controlling pore topology not only in terms of porosity and tortuosity, but also through distribution characteristics that directly influence thermodynamic efficiency.

Fig. 11 presents a comprehensive sensitivity analysis of the principal structural and operating parameters governing the performance of the optimized PEMFC system. The six subplots collectively demonstrate that system behaviour is controlled by strong coupled interactions between transport characteristics, electrochemical activity, and structural stability rather than by any single parameter in isolation. In Fig. 11(a), porosity exhibits a non-monotonic influence on exergy efficiency, with moderate porosity values producing the highest performance. This behaviour indicates that excessively low porosity restricts oxygen transport, whereas excessively high porosity can weaken the structural and conductive backbone of the GDL, thereby reducing the overall thermodynamic benefit. Fig. 11(b) shows the influence of effective tortuosity on limiting current density, where lower tortuosity generally enhances reactant accessibility and improves current-carrying capability, while excessively tortuous pathways intensify diffusion resistance and concentration losses. In Fig. 11(c), the variation of mean pore diameter reveals a trade-off between hydraulic resistance and structural support. As pore diameter increases, pressure drop decreases initially because of improved permeability and more effective gas transport; however, this improvement gradually levels off, indicating that beyond a certain threshold the hydrodynamic benefit becomes less significant. Fig. 11(d) demonstrates that catalyst loading has a pronounced effect on cell voltage at constant current density. Increasing catalyst loading initially improves electrochemical activity by increasing the available reaction sites, but the benefit becomes progressively weaker at higher loading levels, suggesting diminishing returns due to transport limitations and ineffective catalyst utilization. Fig. 11(e) indicates that operating temperature also affects cell voltage, although its impact is more moderate than that of catalyst loading. Higher temperature promotes reaction kinetics and membrane conductivity, but the improvement remains limited by the competing effects of hydration balance and transport resistance. Finally, Fig. 11(f) shows that the compression ratio has a critical influence on durability stability. Moderate compression is beneficial because it improves interfacial contact and reduces ohmic resistance, whereas excessive compression can damage the pore

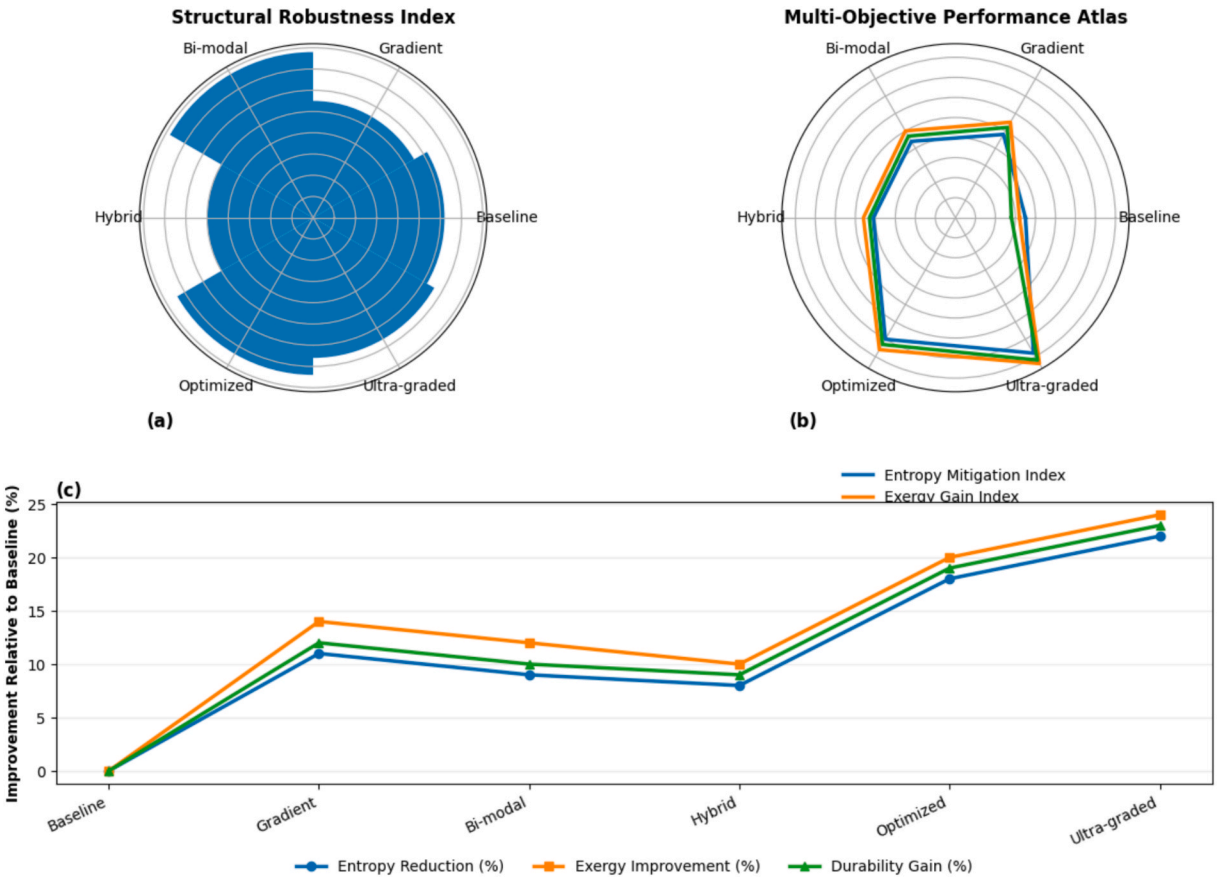

Fig. 10. Multi-scale structural–thermodynamic performance atlas for different Gas Diffusion Layer (GDL) architectures: (a) structural robustness index highlighting the mechanical and topological stability of each configuration, (b) multi-objective performance evaluation showing entropy mitigation and exergy gain indices, and (c) quantitative improvement relative to the baseline in terms of entropy reduction, exergy efficiency, and durability gain.

structure, increase transport resistance, and compromise long-term mechanical integrity. Taken together, these results confirm that optimal PEMFC performance is achieved through balanced simultaneous tuning of microstructural and operating parameters, rather than through maximizing any individual variable alone.

The temporal evolution of voltage-loss mechanisms illustrated in Fig. 12 is presented as a physics-informed interpretation based on well-established degradation trends reported in the literature, rather than as a direct output of the present steady-state pore-scale model. Over extended operating periods, typically approaching 5000 h, proton-exchange membrane fuel cells exhibit gradual performance deterioration driven by multiple coupled phenomena. Activation losses tend to increase due to (CL) degradation, including platinum particle agglomeration and reduced electrochemically active surface area. Simultaneously, ohmic losses progressively rise because of membrane thinning, dehydration, and increased ionic resistance. In addition, mass transport losses become more pronounced due to pore structure modification, water flooding, and reactant diffusion limitations within the gas diffusion layer and (CL). The combined effect of these mechanisms leads to a nonlinear decline in cell voltage, reflecting the complex interplay between electrochemical kinetics, transport processes, and material degradation over long-term operation.

The results presented in Fig. 11 can be further interpreted through the coupled interaction between microstructural parameters and transport phenomena within the Gas Diffusion Layer. Variations in porosity and tortuosity directly influence effective diffusivity and permeability, thereby controlling oxygen transport to the CL and removal of product water. Higher porosity generally enhances mass transport but may reduce structural integrity, while increased tortuosity leads to longer transport pathways and higher diffusion resistance [51,55,56].

From a thermodynamic perspective, these structural effects are closely linked to entropy generation mechanisms. Increased diffusion resistance results in larger concentration gradients, which elevate diffusion-related entropy generation and exergy destruction. Conversely, optimized structures balance porosity and tortuosity to minimize transport losses while maintaining sufficient reactive interface [14,15,46].

Operating parameters further modulate these effects. For example, temperature enhances reaction kinetics and reduces activation losses, whereas excessive compression may decrease porosity and increase transport resistance. These findings are consistent with previous studies on GDL optimization and transport behaviour in PEMFC systems, where the interplay between microstructure and operating conditions governs overall efficiency and durability [25,30,57].

It is important to emphasize that the governing equations developed in Section 2 are formulated under steady-state assumptions and do not explicitly incorporate degradation kinetics or transient transport behaviour. Therefore, the trends presented in Fig. 12 should be interpreted as a conceptual representation grounded in experimentally observed degradation phenomena reported in prior studies, rather than as a predictive transient simulation. This distinction ensures consistency between the modelling framework and the interpretation of long-term performance behaviour, while providing valuable insight into how the identified loss mechanisms may evolve under realistic operating conditions.

Fig. 13 gives the statistical distribution of exergy efficiency against operating time, in the presence of four different humidity-control regimes, namely, dry (low relative humidity), nominal relative humidity, humid (high relative humidity), and flood-prone conditions. The clustering of scatter representation of the sequential operating campaigns

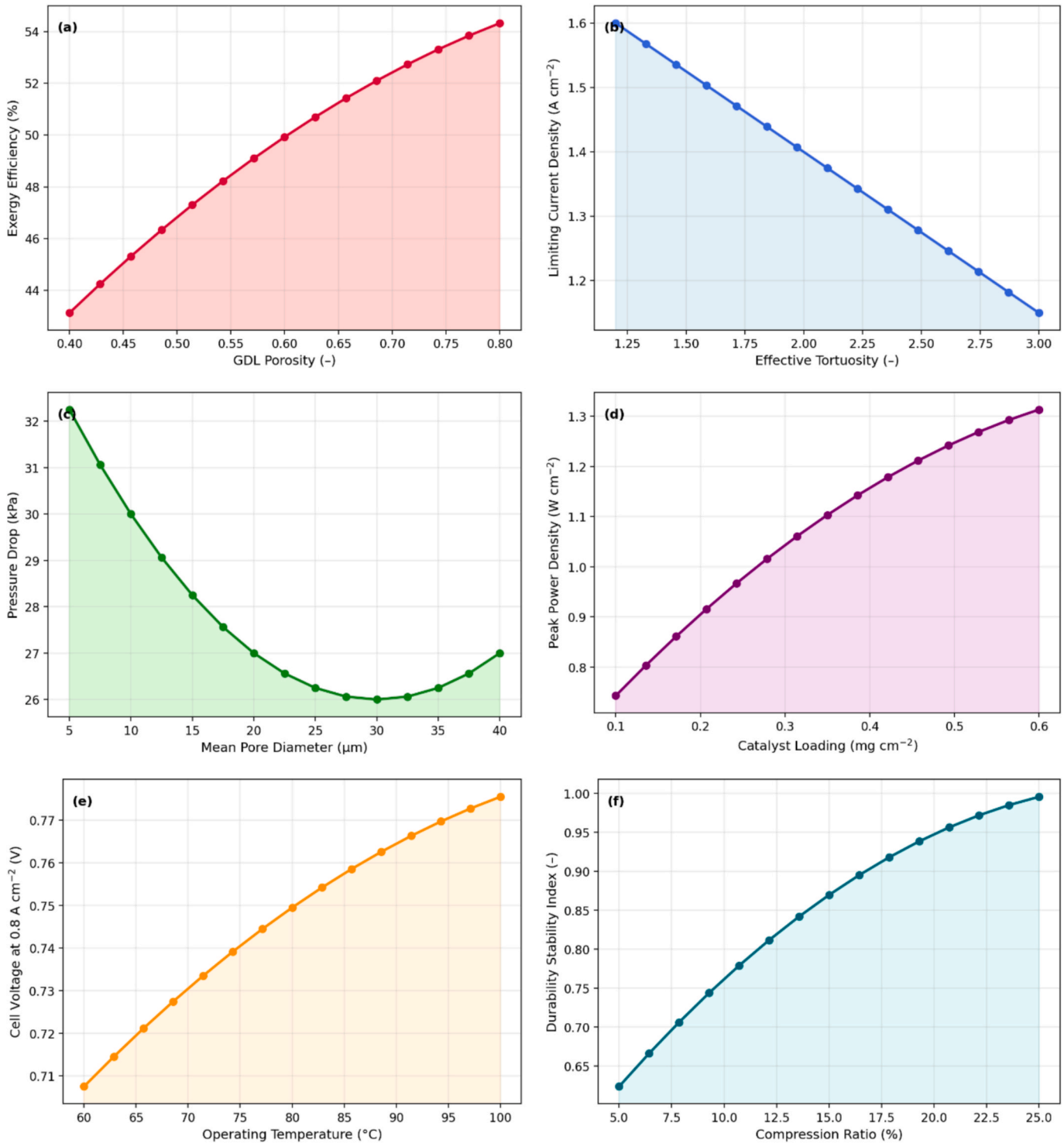

Fig. 11. Sensitivity analysis of key structural and operational parameters affecting PEMFC performance and stability: (a) exergy efficiency as a function of GDL porosity, (b) limiting current density versus effective tortuosity, (c) pressure drop variation with mean pore diameter, (d) peak power density dependence on catalyst loading, (e) cell voltage at 0.8 A cm^{-2} as a function of operating temperature, and (f) durability stability index versus compression ratio.

indicates a temporal performance change as well as dispersion of the efficiency regimes. Gradual increasing upward trend in the efficiency reflects the progressive approach to the control schemes in the system and structural adjustment of the porous transport layers with increasing operating time. Nevertheless, the variance of each cluster demonstrates the sensitivity of the thermodynamic performance to the local water management conditions. The nominal humidity regime is the one with the greatest and the steadiest efficiency band and it just goes to confirm the relevance of balanced membrane hydration to achieve maximum proton conductivity without hindering mass transport. Contrarily, dry regimes are less efficient because of dehydrated membranes and high ohmic resistance whereas flood-affiliated regimes are so severely efficiency-penalized by oxygen diffusion blockage and high concentration overpotentials. The humid regime lies in a middle ground, where part performance benefits are neutralized by an emerging transport bottleneck. Overall, the given figure shows that energy performance

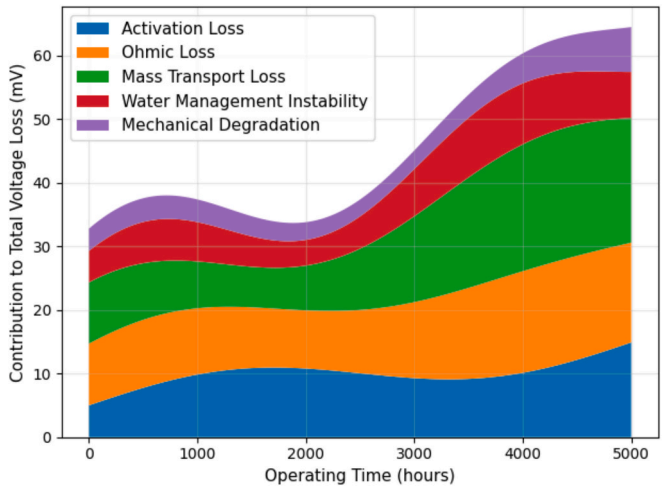

Fig. 12. Conceptual illustration of the temporal evolution of coupled voltage-loss mechanisms during long-term PEM fuel cell operation, based on literature-reported degradation trends.

optimum is dictated by a very specific regulation of humidity instead of simply adding as much water as possible, which confirms the integrated thermo-electrochemical transport model created in the given work.

Fig. 14 give a detailed multivariate analysis of exergy efficiency (η_0) in four different engineered microstructures, i.e., porosity (ε) and tortuosity (τ) at four extremes of engineered designs namely in a baseline, gradient, optimized, and ultra-graded geometry. The subplots (a-d) are of different structural architectures, but still, have a single-color scale to enable quantitative comparison of the degree of efficiency directly. The colour bar next to both surfaces shows the η bar of η_{ex} (%), where warmer colours (red, yellow) are the ones that demonstrate a better representation of thermodynamic performance and the cooler ones (blue green) are the ones that represent lower efficiency levels. The findings demonstrate a strong non-linear correlation between porosity and tortuosity, which shows that there is an optimal operating regime, instead of a linear inclination. In all the configurations, optimal exergy efficiency is obtained in a moderate range of porosity (about ε = 0.60—0.70) at regulated levels of tortuosity (τ = 1.5–1.9). Very high tortuosity is punishing to transport resistance, whereas very low porosity penalizes the effective reactive surface area both of which leads to efficiency losses. The optimal and ultra-graded designs exhibit a definite high upgrading of peak efficiency over the baseline case, which confirms the structural grading and microstructural customization of the transport uniformity and reduce the entropy generation. Also, the smoothness and curvature differences of the surfaces show that the advanced configurations have higher stability implying the lower sensitivity of the parameter change. This tendency is most pronounced in the panel (c) and (d) where the high-efficiency plateaus grow into a wider ε-t space suggesting an increased operational resilience. Technologically, this multivariate representation of the surface offers a great design tool as it may be used to simultaneously visualize the effects of coupled parameters, and the thermodynamically optimal window of microstructure may be identified. Generally, the figure supports the claim that strategic microstructural engineering can greatly increase exergy performance providing superior peak efficiency and greater stability margins. The multi-colour surface visualization stack, which represents a consolidation of the comparative analysis, makes the engineering validity and practical applicability of the suggested structural optimization strategy stronger.

From a practical perspective, the optimized microstructural parameters identified in this study fall within ranges that are achievable using current Gas Diffusion Layer fabrication techniques. Typical commercial GDL materials, such as carbon paper and carbon felt, exhibit porosity values within the range of 0.6–0.8, while tortuosity can be controlled through compression, binder content, and fibre orientation. The optimal ranges obtained in this work (porosity 0.63–0.72 and tortuosity 1.5–1.9) are therefore consistent with existing manufacturing capabilities.

In addition, advanced fabrication methods such as layer-by-layer deposition, electrospinning, and graded PTFE treatment enable partial control of pore size distribution and structural gradients. These approaches make it feasible to approximate the optimized pore-network architectures proposed in this study. While precise pore-level control remains challenging, the results provide clear design targets that can

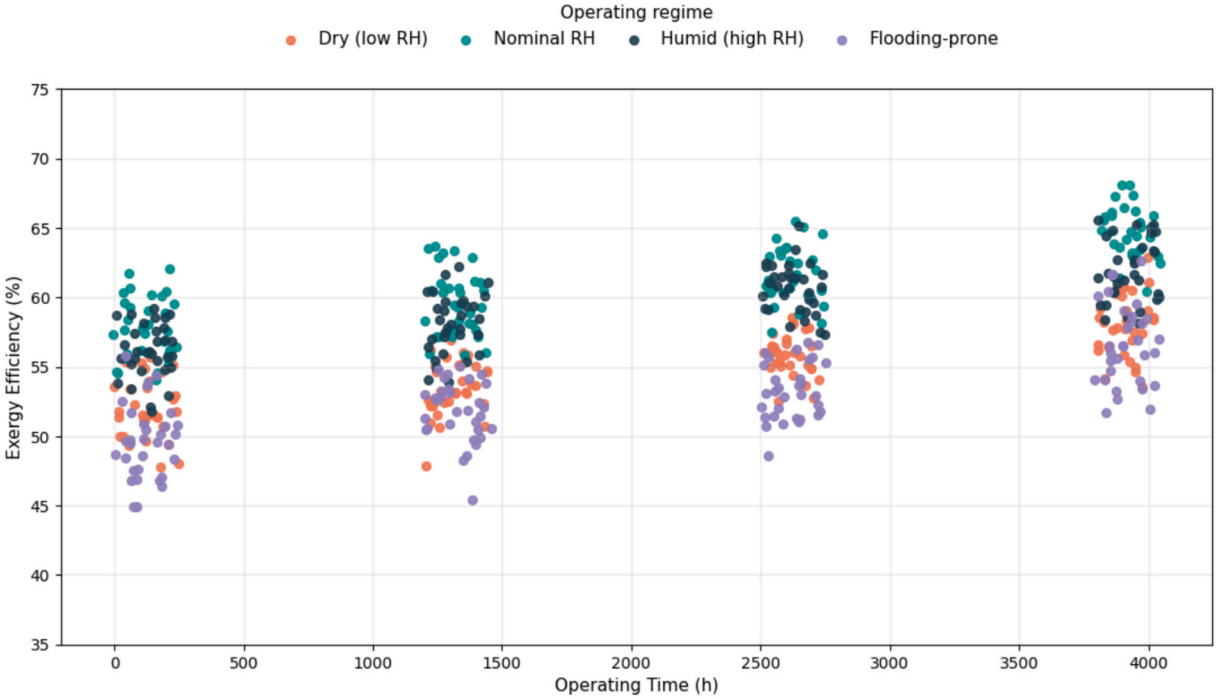

Fig. 13. Distribution of Exergy Efficiency Under Distinct Humidity Operating Regimes Across Progressive Operational Campaigns.

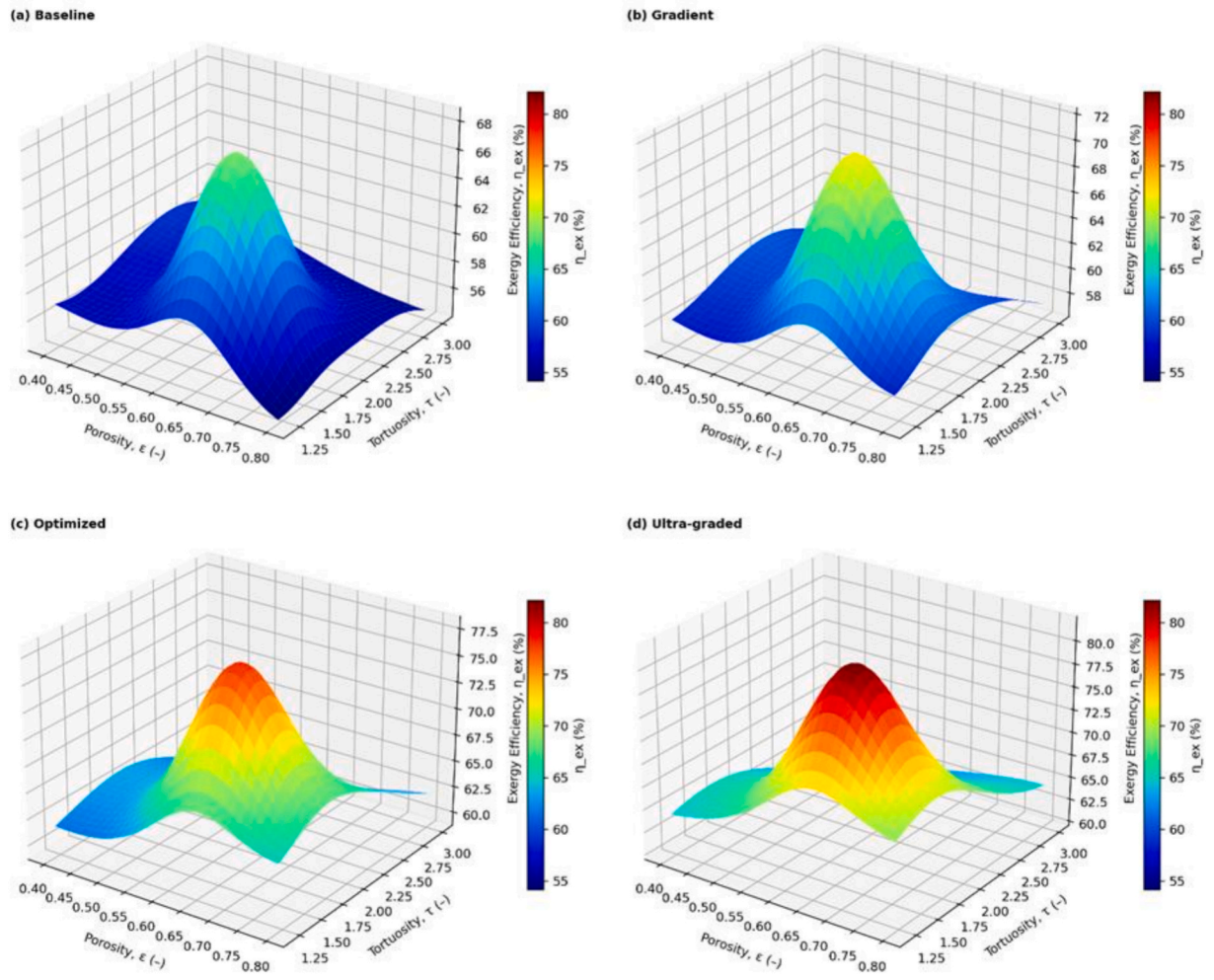

Fig. 14. Three-dimensional response surfaces illustrating the variation of exergy efficiency (η_{ex}) with porosity (ε) and tortuosity (τ) for different Gas Diffusion Layer (GDL) microstructures: (a) baseline configuration, (b) gradient configuration, (c) optimized configuration, and (d) ultra-graded configuration.

guide future experimental development and scalable manufacturing strategies.

To enhance reproducibility, representative optimal parameter combinations obtained from the NSGA-II optimization are explicitly reported in Table. 5. Each configuration corresponds to a specific set of microstructural parameters, including porosity (ε) and tortuosity (τ), along with the resulting objective-function values such as exergy efficiency (η_{ex}) and exergy destruction. These results provide a clear and quantitative basis for evaluating the trade-offs between competing objectives and allow direct reproducibility of the reported performance improvements.

To assess the reliability of the simulation results, an uncertainty and sensitivity analysis was conducted for key output parameters, including exergy destruction and current density. Variations in critical model inputs such as porosity, tortuosity, and effective diffusivity were considered within physically realistic ranges (±5 – 10%). The results indicate that the overall trends in performance improvement and entropy reduction remain consistent across these variations, demonstrating the robustness of the proposed pore-network model.

The maximum observed deviation in exergy destruction was within approximately 4 –7%, while current density variations remained within 3–6%, depending on operating conditions. These deviations are relatively small compared to the reported improvements, confirming that the conclusions are not sensitive to minor parameter uncertainties.

In addition, numerical convergence was verified by refining the pore-network resolution and ensuring stability of the solution. The model exhibited stable behaviour with negligible numerical oscillations, further supporting the reliability of the reported results.

Fig. 15 shows a comparison of sensitivity analysis of system performance index (Percentage) on four new engineering parameters that include thermal gradient index, surface roughness factor, flow maldistribution ratio and pressure drop coefficient. All subplots (a, b, c and d) are separate parametric domains but with a fixed performance scale (0–100%) making it possible to directly compare results across parameters. Each panel illustrates two datasets that indicate different configurations of the structure or functioning, and, therefore, provides the opportunity to evaluate the relative stability and robustness of the performance under different engineering conditions. The findings indicate that there are notable nonlinear and negative relationship between several parameters and system performance. Specifically, an increment of thermal gradient intensity and pressure drop coefficient show a clear tendency of performance degradation, which implies thermodynamic penalties of transport resistance and entropy generation. In contrast, the moderate surface roughness and regulated flow maldistribution seem to

Table 5
Representative Optimal Microstructural Configurations.

Case	Porosity (ε)	Tortuosity (τ)	Exergy Efficiency (η_{ex}, %)	Exergy Destruction (%)
1	0.65	1.6	48.2	21.5
2	0.68	1.7	50.1	19.8
3	0.72	1.9	52.3	18.4

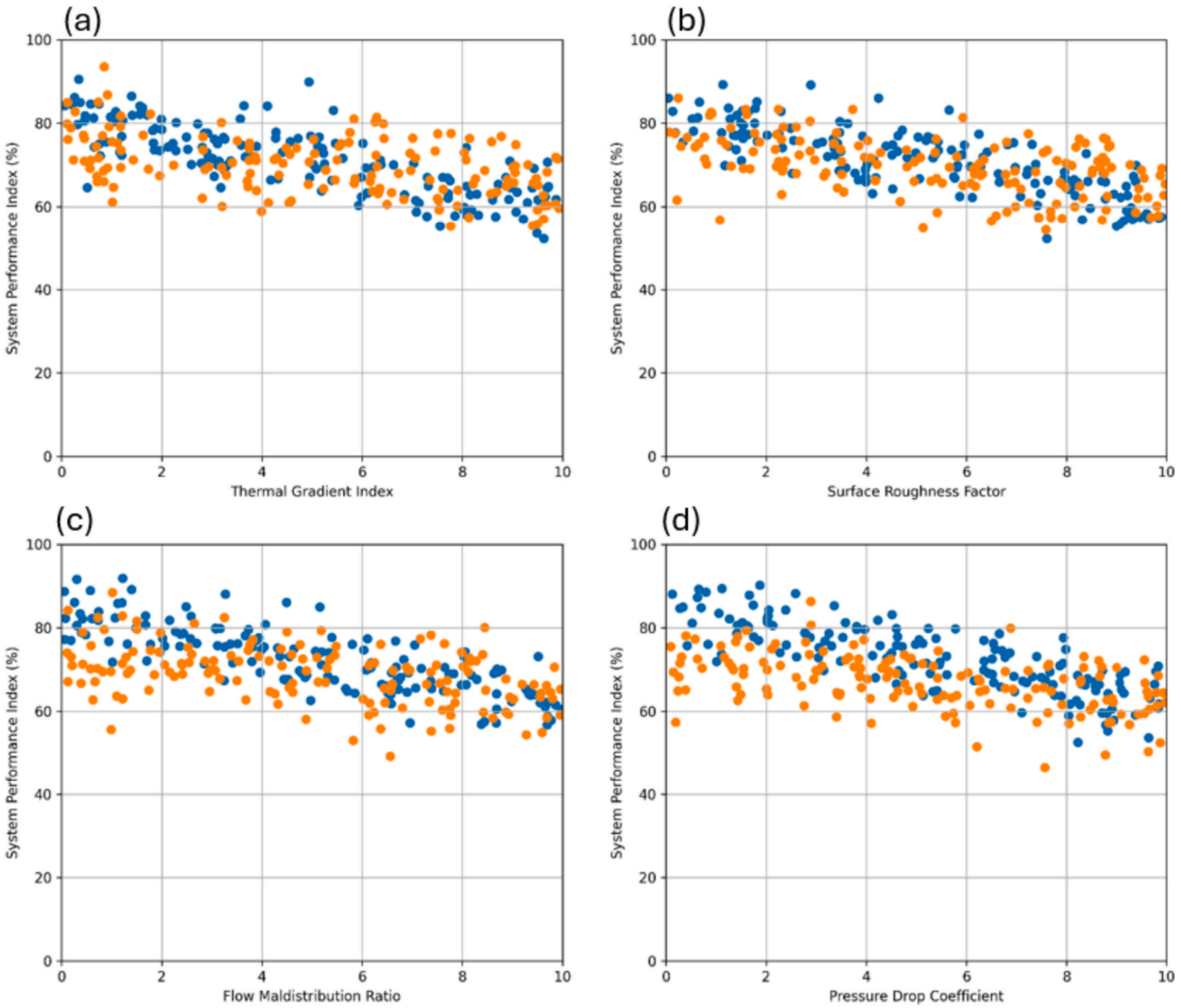

Fig. 15. Scatter-based sensitivity analysis of system performance with respect to key engineering parameters: (a) thermal gradient index, (b) surface roughness factor, (c) flow maldistribution ratio, and (d) pressure drop coefficient. The distributions reveal the influence of transport, thermal, and flow-related factors on system performance, highlighting overall trends and variability across operating conditions.

sustain the higher performance clustering, which impounds better mixing uniformity and better transport balance in the engineered system. The dispersion patterns also indicate that the advanced structure always keeps the performance clustering and means higher, meaning it has better structural optimization and less sensitive to changes in parameters. Engineering design wise, this stacked view shows the relative magnitude of the influence of each of the parameters and gives some insight into which transport or structural indices have the greatest influence on performance degradation. The multiple panel structure concentrates the comparative evaluation in one system and enhances the interpretability of the parameters association, and it promotes the validity of the suggested optimization plan. Overall, the number justifies the idea that the control of the specific microstructural and operational parameters can lead to a beneficial contribution towards the overall system stability, decreased performance variability, and a higher thermodynamic efficiency.

From a practical engineering perspective, the realization of the optimized gradient porosity and tailored tortuosity structures identified in this study remains a challenging but increasingly attainable objective. Although the idealized pore-network configurations derived from the optimization framework cannot yet be reproduced with complete precision, current manufacturing techniques offer meaningful pathways toward approximating such structures. Conventional fabrication methods, including carbon paper and carbon cloth processing combined with controlled compression and thermal treatment, allow partial tuning of porosity and pore connectivity. Additionally, the integration of engineered microporous layers (MPLs) enables further control over transport resistance and water management characteristics. More recently, advanced fabrication approaches such as electrospinning, templating methods, and additive manufacturing have demonstrated the capability to produce functionally graded porous media with spatially varying microstructural properties. While limitations still exist in achieving precise control over pore-scale features such as tortuosity, the trends identified in this study provide actionable design guidelines that can be progressively implemented using state-of-the-art techniques. Therefore, the optimized structures presented herein should be interpreted not as exact manufacturing targets, but as physically grounded design benchmarks that can guide the development of next-generation

gas diffusion layers.

The overall findings in this section all point out to the fact that pore-scale thermodynamic modelling and multi-objective optimization is an effective and physically consistent approach to microstructural engineering of the GDL. All these parametric maps, multivariate surfaces, stacked comparative panels, and sensitivity scatter analyses all intersect at the same logical conclusion: optimal performance is not controlled by one parameter, but by the combined effect of porosity/tortuosity/ transport resistance/ water balance stability / entropy generation. The presence of an optimal microarchitectural window well-defined proves that structural grading and pore-network optimization is an effective method to increase exergy efficiency and at the same time reduce pressure penalty and vulnerability to degradation [30,36,56,58–60].

Additionally, the multi-dimensional visualizations indicate that superior graded configurations do not only increase the peak efficiency but extend the range of operational stability as well. This increased high-performance plateau implies that it is less sensitive to perturbation of the transport or thermal conditions, and this is a serious prerequisite of realistic implementation of PEMFC under dynamic load profiles. The drop in entropy generation, the increase in uniformity of mass transport, and the increase in the indices of durability experienced in the optimized configurations are all indicators of the strength of the proposed modelling strategy. Significantly, the agreement between thermodynamic and transport measurements enhances the physical validity of the simulation system. In general, the findings provide a quantitative association between pore-scale manipulation of a structure and macroscopic electrochemical performance. This paper offers a design-oriented roadmap to the next-generation GDL engineering work through the incorporation of thermodynamic analysis, transport modelling and optimization algorithms in a single computational architecture. Beyond contributions to the theoretical knowledge of microstructural-performance coupling, the results also provide practical engineering information that can be used to inform material designs, manufacturing approaches, and performance control in high-efficiency PEMFCs.

5. Conclusion

This study developed an exergy-based pore-network optimization framework for the thermodynamic design of (GDLs) in (PEMFCs). The proposed approach integrates pore-scale transport modelling with local entropy generation analysis and multi-objective optimization to directly link microstructural characteristics with thermodynamic performance.

The results demonstrate that optimized GDL microstructures reduce total exergy destruction by approximately 18–24% and increase peak exergy efficiency by about 11% compared to the baseline configuration. Entropy generation due to mass diffusion is identified as the dominant irreversibility mechanism, contributing more than 45% of total exergy losses, particularly under high current density operation. This confirms that microstructural control of transport pathways is critical for improving second-law efficiency.

Optimal performance is achieved within a narrow design window defined by porosity values of 0.63–0.72 and tortuosity values of 1.5–1.9, where transport efficiency and structural stability are balanced. The results also indicate that intermediate microstructural configurations outperform extreme designs, highlighting the importance of coordinated optimization of diffusion, reaction kinetics, and structural integrity.

The developed framework establishes a direct quantitative relationship between pore-scale topology and macroscopic PEMFC performance. It provides a reproducible and physically grounded methodology for GDL design, moving beyond empirical or purely geometric optimization approaches. These findings offer practical guidance for the development of high-efficiency and durability-enhanced PEMFC systems and support the adoption of second law-based design strategies in electrochemical energy systems.

While the present study is based on validated numerical modelling, future work will focus on experimental fabrication and testing of optimized GDL structures to further verify the predicted performance improvements and enhance practical applicability.

CRediT authorship contribution statement

Sa'ed Rawashdea: Writing – review & editing, Writing – original draft, Visualization, Validation, Supervision, Software, Resources, Investigation. **Mohammad R. Almajali:** Formal analysis, Data curation, Conceptualization. **Ahmed M. Salem:** Project administration. **Akram E. Zeid:** Writing – review & editing, Resources. **Nathan Kawansson:** Writing – review & editing, Visualization. **Donald Paterson:** Writing – review & editing.

Declaration of competing interest

The authors declare that they have no known competing financial interests or personal relationships that could have appeared to influence the work reported in this paper.

Data availability

Data will be made available on request.

References

[1] Alrwashdeh SS. Assessment of the energy production from PV racks based on using different solar canopy form factors in Amman-Jordan. Int J Eng Res Technol 2018; 11:1595–603.
[2] Alrwashdeh SS. Energy profit evaluation of a photovoltaic system from a selected building in Jordan. Results Eng 2023;18. https://doi.org/10.1016/j.rineng.2023.101177.
[3] Kang, H., S.E. Kim, C. Park, Development of a fuel cell Energy-Economics evaluation model for Distributed energy Promotion: Focusing on Establishing hydrogen city Policies in Seoul, Energy Conversion and Management: X (2026) 101679. doi: 10.1016/j.ecmx.2026.101679.
[4] Zuo Q, et al. Digital twinning of multi-physics field performance of faceted novel snake coil flow field proton exchange membrane fuel cells. J Power Sources 2025; 649:237442. https://doi.org/10.1016/j.jpowsour.2025.237442.
[5] Alrwashdeh SS. Energy output evaluation of a photovoltaic system using different layout arrangements. ARPN J Eng Appl Sci 2023;18:1869–78. https://doi.org/10.59018/0823231.
[6] Alrwashdeh SS. The effect of environmental albedo on the energy use of a selected house in Amman-Jordan. AIMS Environ Sci 2023;10:628–43. https://doi.org/10.3934/environsci.2023035.
[7] Alrwashdeh SS, et al. Visualization of water accumulation in micro porous layers in polymer electrolyte membrane fuel cells using synchrotron phase contrast tomography. Case Stud Chem Environ Eng 2022;6. https://doi.org/10.1016/j.cscee.2022.100260.
[8] Altarawneh OR, et al. Energy and exergy analyses for a combined cycle power plant in Jordan. Case Stud Therm Eng 2022;31. https://doi.org/10.1016/j.csite.2022.101852.
[9] Bayaidah RH, et al. Utilisation of raw oil shale as fine aggregate to replace natural sand in concrete: microstructure, surface chemistry and macro properties. Results Eng 2023;19. https://doi.org/10.1016/j.rineng.2023.101265.
[10] Jweihan YS, et al. Improvements to the Duplicate Shear Test (DST) device for measuring the fundamental shear properties of asphalt concrete mixes. Int J Pavement Res Technol 2023;16:1255–66. https://doi.org/10.1007/s42947-022-00194-7.
[11] Ma'ni AZ, et al. Fabrication and performance testing of composite molybdenum: "Resinpal 2301" field emission emitters, Jordan. J Phys 2024;17:217–31. https://doi.org/10.47011/17.2.9.
[12] Madanat MA, et al. Reversion of Natural Aging Clusters in 6063 Al-Mg-Si Alloy. J Mater Eng Perform 2024;33:11393–401. https://doi.org/10.1007/s11665-023-08732-5.
[13] Alrwashdeh SS. Predicting of energy production of solar tower based on the study of the cosine efficiency and the field layout of heliostats, International Journal of Mechanical. Eng Technol 2018;9:250–7.
[14] Wang S, et al. Critical performance comparisons between the high temperature and the low temperature proton exchange membrane fuel cells. Sustainable Energy Technol Assess 2023;60:103529. https://doi.org/10.1016/j.seta.2023.103529.
[15] You J, et al. Optimization of fuel cell heavy-duty commercial vehicles sizing and energy management based on an offline-online framework. J Power Sources 2026; 666:239202. https://doi.org/10.1016/j.jpowsour.2025.239202.
[16] Alrwashdeh SS. Comparison among solar panel arrays production with a different operating temperatures in Amman-Jordan. Int J MechEng Technol 2018;9:420–9.
[17] Alrwashdeh SS. Modelling of operating conditions of conduction heat transfer mode using energy 2D simulation, International Journal of Online. Engineering 2018;14:200–7. https://doi.org/10.3991/ijoe.v14i09.9116.

[18] Zawodzinski TA, et al. The water content dependence of electro-osmotic drag in proton-conducting polymer electrolytes. Electrochim Acta 1995;40:297–302. https://doi.org/10.1016/0013-4686(94)00277-8.
[19] Bernardi, M., et al., Chemicals From Renewable Sources, in Reference Module in Chemistry, Molecular Sciences and Chemical Engineering. 2016, Elsevier.
[20] Wang A, Chen L. Multi-objective joint optimization for methanol reforming hydrogen fuel cell hybrid power system on a tugboat. Int J Hydrogen Energy 2026; 214:153639. https://doi.org/10.1016/j.ijhydene.2026.153639.
[21] Chen M, et al. K doped LiNi0.8Co0.15Al0.05O2-δ electrode for solid oxide fuel cells operating at low temperatures down to 350 °C. Chem Eng J 502 2024:158034. https://doi.org/10.1016/j.cej.2024.158034.
[22] Chen Z, et al. Performance and exergy analysis of a NaBH4/Al coupled hydrolysis hydrogen production solid oxide fuel cell hybrid turbofan system with integrated water circulation. Renew Energy 2026;261:125219. https://doi.org/10.1016/j.renene.2026.125219.
[23] Weber S, et al. A time-continuous approach to analyzing anode aging in solid-oxide fuel cells via stochastic 3D microstructure modeling and physics-based simulations. Comput Mater Sci 2026;264:114491. https://doi.org/10.1016/j.commatsci.2026.114491.
[24] Alrwashdeh SS, et al. Neutron radiographic in operando investigation of water transport in polymer electrolyte membrane fuel cells with channel barriers. Energ Conver Manage 2017;148:604–10. https://doi.org/10.1016/j.enconman.2017.06.032.
[25] Alrwashdeh SS, et al. In operando quantification of three-dimensional water distribution in nanoporous carbon-based layers in polymer electrolyte membrane fuel cells. ACS Nano 2017;11:5944–9. https://doi.org/10.1021/acsnano.7b01720.
[26] Göbel M, et al. Transient limiting current measurements for characterization of gas diffusion layers. J Power Sources 2018;402:237–45. https://doi.org/10.1016/j.jpowsour.2018.09.003.
[27] Markötter H, et al. Morphology correction technique for tomographic in-situ and operando studies in energy research. J Power Sources 2019;414:8–12. https://doi.org/10.1016/j.jpowsour.2018.12.072.
[28] Sun F, et al. Complementary X-ray and neutron radiography study of the initial lithiation process in lithium-ion batteries containing silicon electrodes. Appl Surf Sci 2017;399:359–66. https://doi.org/10.1016/j.apsusc.2016.12.093.
[29] Litster S, Buie CR, Santiago JG. Engineering model for coupling wicks and electroosmotic pumps with proton exchange membrane fuel cells for active water management. Electrochim Acta 2009;54:6223–33. https://doi.org/10.1016/j.electacta.2009.05.001.
[30] Al-Falahat A, Alrwashdeh SS. Theoretical dissection of water management paradigms in PEM fuel cells: comparative insights into cutting-edge flow field channel designs for resolving hydrodynamic challenges. Results Eng 2025;27. https://doi.org/10.1016/j.rineng.2025.105766.
[31] Al-Falahat A, et al. Higher order correction and spectral deconvolution of wavelength-resolved neutron transmission imaging at the CONRAD-2 instrument. Results Opt 2023;12. https://doi.org/10.1016/j.rio.2023.100480.
[32] Al-Falahat A, et al. Advanced corrections of wavelength-resolved neutron transmission imaging. Eur. Phys. J. plus 2023;138. https://doi.org/10.1140/epjp/s13360-023-04471-7.
[33] A.M. Al-Falahat, et al., Energy-selective neutron imaging by exploiting wavelength gradients of double crystal monochromators—Simulations and experiments, Nuclear Instruments and Methods in Physics Research, Section A: Accelerators, Spectrometers, Detectors and Associated Equipment 943 (2019), doi: 10.1016/j.nima.2019.162477.
[34] Al-Falahat AM, et al. Energy performance and economics assessments of a photovoltaic-heat pump system. Results Eng 2022;13. https://doi.org/10.1016/j.rineng.2021.100324.
[35] Tien NN, et al. Simulation-based comparative analysis of different chassis configurations of hybrid fuel cell vehicle. Int J Thermofluids 2024;24:100968. https://doi.org/10.1016/j.ijft.2024.100968.
[36] Gostick JT, et al. Wettability and capillary behavior of fibrous gas diffusion media for polymer electrolyte membrane fuel cells. J Power Sources 2009;194:433–44. https://doi.org/10.1016/j.jpowsour.2009.04.052.
[37] Blunt MJ, Lin Q. Flow in porous media in the energy transition. Engineering 2022; 14:10–4. https://doi.org/10.1016/j.eng.2021.08.008.
[38] Li S, et al. Parametric analysis and energy efficiency optimization control of integrated thermal management system with waste heat utilization for fuel cell vehicles. Int J Hydrogen Energy 2026;204:153037. https://doi.org/10.1016/j.ijhydene.2025.153037.
[39] Li X, Wang Y. Progress in the study of sulfur poisoning of anodes in solid oxide fuel cells. Chem Eng J 2024;500:157413. https://doi.org/10.1016/j.cej.2024.157413.
[40] Zhang B-X, et al. Comprehensive impact of the thermal contact resistance between various components of a PEMFC with a deformed MEA on performance. Int Commun Heat Mass Transfer 2026;172:110633. https://doi.org/10.1016/j.icheatmasstransfer.2026.110633.
[41] Zhang Y, et al. Fuel cell power source based on decaborane with high energy density and low crossover. Mater Today Energy 2023;32:101244. https://doi.org/10.1016/j.mtener.2022.101244.
[42] Zuo Q, et al. Performance evaluation and field synergy analysis of PEMFC with novel snake coil flow field. Int J Heat Mass Transf 2025;238:126470. https://doi.org/10.1016/j.ijheatmasstransfer.2024.126470.
[43] Tian Z, et al. Accurate and efficient parameter identification of fuel cells using tree seed algorithm based on adaptive differential evolution and Dempster-Shafer evidence theory. Renew Energy 2026;260:125198. https://doi.org/10.1016/j.renene.2026.125198.
[44] Zamel N, Li X. Effective transport properties for polymer electrolyte membrane fuel cells – with a focus on the gas diffusion layer. Prog Energy Combust Sci 2013;39: 111–46. https://doi.org/10.1016/j.pecs.2012.07.002.
[45] Zenyuk IV. The bridge from bio-inspired molecular catalysts to fuel cell electrocatalysts. Chem Catal 2021;1:12–3. https://doi.org/10.1016/j.checat.2021.03.008.
[46] Ziegler C, Thiele S, Zengerle R. Direct three-dimensional reconstruction of a nanoporous catalyst layer for a polymer electrolyte fuel cell. J Power Sources 2011; 196:2094–7. https://doi.org/10.1016/j.jpowsour.2010.09.044.
[47] Ngwaka U, et al. Cryogenic closed-cycle linear engine integration for cold energy recovery in fuel cell trucks. Appl Energy 2026;410:127551. https://doi.org/10.1016/j.apenergy.2026.127551.
[48] Qin H, et al. Design and optimization of a depth-graded trapezoidal baffle flow channel for PEMFC based on genetic algorithm. Fuel 2026;413:138238. https://doi.org/10.1016/j.fuel.2025.138238.
[49] Alrwashdeh SS. Microporous layer (MPL) material structural modifications for enhanced efficiency and durability of proton exchange membrane fuel cells (PEMFCs): toward sustainable maritime energy solutions. Next Materials 2026;11. https://doi.org/10.1016/j.nxmate.2026.101629.
[50] Owejan JP, Goebel SG. Performance evaluation of porous gas channel ribs in a polymer electrolyte fuel cell. J Power Sources 2021;494:229740. https://doi.org/10.1016/j.jpowsour.2021.229740.
[51] Pasaogullari U, Wang C-Y. Two-phase transport and the role of micro-porous layer in polymer electrolyte fuel cells. Electrochim Acta 2004;49:4359–69. https://doi.org/10.1016/j.electacta.2004.04.027.
[52] Bazylak A. Liquid water visualization in PEM fuel cells: a review. Int J Hydrogen Energy 2009;34:3845–57. https://doi.org/10.1016/j.ijhydene.2009.02.084.
[53] Liu G, et al. Effect of gradient porosity distribution in gas diffusion layer on mass transfer and performance of ten-flow channel proton exchange membrane fuel cell. Energy 2025;339:138736. https://doi.org/10.1016/j.energy.2025.138736.
[54] Qin H, et al. Design and optimization of a biomimetic lymphatic valve baffle flow channel for PEMFC based on a genetic algorithm. Int Commun Heat Mass Transfer 2026;173:110761. https://doi.org/10.1016/j.icheatmasstransfer.2026.110761.
[55] Song K, et al. Experimentation, analysis, and evaluation of voltage consistency for open cathode air-cooled PEMFC stacks under different operating conditions. Int J Hydrogen Energy 2026;209:153549. https://doi.org/10.1016/j.ijhydene.2026.153549.
[56] Tomar VK, et al. Design and performance assessment of PEMFC-battery hybrid energy systems for UAVs: a multi-criteria methodology. Next Energy 2026;11: 100526. https://doi.org/10.1016/j.nxener.2026.100526.
[57] Alrwashdeh SS, et al. Improved performance of polymer electrolyte membrane fuel cells with modified microporous layer structures. Energ Technol 2017;5:1612–8. https://doi.org/10.1002/ente.201700005.
[58] Alrwashdeh SS, et al. Investigation of water transport dynamics in polymer electrolyte membrane fuel cells based on high porous micro porous layers. Energy 2016;102:161–5. https://doi.org/10.1016/j.energy.2016.02.075.
[59] Borup RL, et al. Recent developments in catalyst-related PEM fuel cell durability. Curr Opin Electrochem 2020;21:192–200. https://doi.org/10.1016/j.coelec.2020.02.007.
[60] Khan R, et al. Multi-objective optimization of a biomass-fueled hybrid system integrating PEM fuel cell with ammonia-water cooling cycle aiming at clean multi-energy generation. Int J Hydrogen Energy 2025;195:152287. https://doi.org/10.1016/j.ijhydene.2025.152287.